

Bachelor Thesis

# Characterizing the Performance of an Unbinned Likelihood Analysis Using Data from the IceCube Neutrino Observatory

Annette Bremer

Würzburg, October 2, 2024



Julius-Maximilians-Universität Würzburg

Faculty of Physics and Astronomy

Chair for Astronomy

Supervisor: Prof. Dr. Sara Buson



---

# Abstract

High-energy astrophysical neutrinos were discovered in 2013 [1] and investigated since 16 years. They are formidable astrophysical messengers that allow to track the sites of origin of cosmic rays.

One motivation to find neutrino point sources is to verify hadronic processes. `IceCubePy` is a python based analysis software under development for the search of point sources in the 10-year point source neutrino public dataset released by the IceCube collaboration using an unbinned likelihood ratio test. This thesis studies the performance of this analysis method by estimating key quantities such as sensitivity flux, the  $3\sigma$  and  $5\sigma$  discovery potential flux and the bias in the reconstruction of the number of signal neutrinos  $n_S$  and the spectral index  $\gamma$ . Simulations of point sources at 21 positions equally spaced in  $\sin\delta$  with declination  $-81^\circ \leq \delta \leq 81^\circ$  and a true spectral index  $\gamma = 2.0$  and  $\gamma = 3.0$ , respectively, are used.

The `IceCubePy` sensitivity and the  $5\sigma$  discovery potential flux as a function of the declination generally follow the trend of the respective quantities published by the IceCube collaboration [2]. Due to differences between the public dataset and the full data available to the IceCube collaboration, there are deviations from the reference. Since `IceCubePy` has been originally developed for a split analysis of the northern and southern neutrino data, the performance around the horizon ( $\delta = -5^\circ$ ) is not optimized. That leads to a worse sensitivity near the horizon compared to the sensitivity published by the IceCube collaboration. The `IceCubePy`  $3\sigma$  discovery potential flux follows the declination dependence of the `IceCubePy`  $5\sigma$  discovery potential flux while corresponding to lower flux values. For  $\gamma = 3.0$ , the `IceCubePy` sensitivity and  $5\sigma$  discovery potential flux are comparable to the respective quantities published by the IceCube collaboration. There is not such a trend in the data sample with  $\gamma = 2.0$ .

The number of signal neutrinos is mostly overestimated for a source with simulated spectral index  $\gamma = 2.0$  but underestimated for  $\gamma = 3.0$ . The bias changes with the declination. The difference between the spectral indices is attributed to different distributions of the angular separation of the simulated signal neutrinos and the true source position. The fitted spectral index converges to a value close to the true spectral index for increasing true numbers of signal neutrinos in both samples. These biases agree within their uncertainty

with the biases shown by T. Glauch [3] for the IceCube collaboration analysis.

# Zusammenfassung

Im Rahmen der Multi-Messenger Astronomie spielen Neutrinos eine wichtige Rolle, da sie Hinweise auf den Ursprung kosmischer Strahlung geben können. Außerdem kann man durch den Nachweis von Neutrino-Emission hadronische Strahlungsprozesse in der Quelle beweisen. Diese Arbeit beschreibt die potentiellen Entstehungsprozesse von kosmischen Neutrinos und mögliche Quellen dieser. Außerdem wird die Funktionsweise des IceCube Neutrino Observatoriums beschrieben.

In dieser Arbeit wird die Leistung der Analysesoftware `IceCubePy` untersucht. `IceCubePy` ist in Python geschrieben und verwendet einen ungebinnten Likelihood-Ratio-Test um Punktquellen im öffentlichen Datensatz des IceCube Neutrino Observatoriums, der 10 Jahre umfasst, zu finden. Die Software befindet sich noch in der Entwicklung, in dieser Arbeit wird die Version v0.28.1 verwendet. Diese Arbeit untersucht die Sensitivität und das Entdeckungspotential sowie den Fit Bias der Anzahl an Signal-Neutrinos sowie des Spektralindex. Dafür wurden zwei Datensätze simuliert, die Punktquellen an verschiedenen Deklinationen enthalten, mit den Spektralindizes  $\gamma = 2.0$  und  $\gamma = 3.0$ .

Zur Berechnung des Sensitivitätsflusses und des Flusses des  $3\sigma$  und  $5\sigma$  Entdeckungspotentials wurde für jeden injizierten Fluss der Anteil an Simulationen berechnet, bei denen der  $TS$ -Wert einen bestimmten Schwellenwert überschreitet. An diesen Anteil als Funktion des injizierten Flusses wurde eine Exponentialfunktion (Sensitivität) oder eine Sigmoidfunktion (Entdeckungspotential) gefittet. Diese Schwellenwerte wurden aus einem Datensatz an Hintergrundsimulationen berechnet. Die so berechneten Flüsse für die Sensitivität und das  $5\sigma$  Entdeckungspotential von `IceCubePy` wurden verglichen mit den Werten der Analyse der IceCube Kollaboration [2]. Die `IceCubePy` Flüsse folgen im Allgemeinen dem Trend der Analyse der IceCube Kollaboration. Da die Instrument Response Function des IceCube Detektors nur in drei Bins veröffentlicht wurde, sind Abweichungen an den Grenzen der Bins zu sehen. `IceCubePy` kann die simulierten Punktquellen nahe des Horizonts von IceCube  $\delta = -5^\circ$  aufgrund des Designs der Analyse nicht korrekt rekonstruieren.

Im zweiten Teil der Arbeit wird der Fit Bias der gefitteten Parameter  $n_S$  und  $\gamma$  untersucht. Der Zusammenhang zwischen der gefitteten Anzahl an Signal-Neutrinos und deren wahrer Anzahl kann durch eine lineare Funktion beschrieben werden. Die hier präsentierten Ergebnisse stimmen im Rahmen ihrer Unsicherheit mit dem Fit Bias der IceCube Analyse überein, die von T. Glauch [3] untersucht wurden. Dieser Bias kann durch die Steigung des linearen Fits quantisiert werden. Die beiden untersuchten Datensätze mit den Spektralindizes  $\gamma = 2.0$  und  $\gamma = 3.0$  verhalten sich sehr ähnlich als Funktion von der Deklination, aber der Datensatz mit  $\gamma = 3.0$  zeigt eine globale Verschiebung zu geringeren Steigungen im Vergleich zum anderen Datensatz. Diese Verschiebung könnte durch einen Unterschied in der Verteilung der Winkelabstände zwischen den injizierten Neutrinos und der wahren Position der simulierten Punktquelle erklärt werden. Um diese Hypothese zu prüfen, werden mehr Untersuchungen benötigt. Der gefittete Spektralindex konvergiert zu einem konstanten Wert nahe des wahren Spektralindex für eine zunehmende Anzahl an Signal-Neutrinos. Das gilt für alle untersuchten Positionen und beide injizierten Spektralindizes. Die hier untersuchte Version `IceCubePy v0.28.1` zeigt Probleme in der Interpolation des Spektralindex, da die Software meistens nur diskrete Werte für den gefitteten Index angibt und nicht kontinuierliche Werte. Das kann durch die Verwendung eines langsameren Interpolators behoben werden. Trotz dieser Einschränkung stimmen die hier gezeigten Ergebnisse im Rahmen ihrer Unsicherheiten mit den Ergebnissen überein, die T. Glauch zeigt [3].

# Contents

<b>1</b>	<b>Multi-Messenger Astronomy</b>	<b>1</b>
1.1	Cosmic Rays . . . . .	3
1.2	Neutrinos . . . . .	4
1.3	Candidate Sources . . . . .	5
1.3.1	Active Galactic Nuclei . . . . .	6
<b>2</b>	<b>IceCube Neutrino Observatory</b>	<b>8</b>
2.1	Detection Interactions . . . . .	10
2.2	Event Morphology . . . . .	11
2.3	IceCube 10-Year Dataset . . . . .	12
2.4	Atmospheric Background . . . . .	14
<b>3</b>	<b>Statistical Methods</b>	<b>16</b>
3.1	Unbinned Likelihood Ratio Test . . . . .	16
3.2	Signal and Background PDF . . . . .	18
3.3	Sensitivity and Discovery Potential . . . . .	19
<b>4</b>	<b>Evaluation of the IceCubePy Performances</b>	<b>21</b>
4.1	Sensitivity and Discovery Potential . . . . .	23
4.1.1	Sensitivity curve for $\gamma = 2.0$ . . . . .	26
4.1.2	Sensitivity curve for $\gamma = 3.0$ . . . . .	29
4.2	Reconstruction of Spectral Parameters . . . . .	30
4.2.1	Observed vs True Number of Events . . . . .	31
4.2.2	Observed vs True Spectral Index . . . . .	34
<b>5</b>	<b>Conclusion and Outlook</b>	<b>36</b>
<b>A</b>	<b>Fit Bias Plots</b>	<b>42</b>





# Chapter 1

## Multi-Messenger Astronomy

The first astronomical observations were done in the optical band with the naked eye before telescopes were invented in the 17th century [4]. In the 20th century, the window for observations in the electromagnetic spectrum expanded with the development of multi-wavelength astronomy. In 1933, K. G. Jansky [5] detected the first extraterrestrial radio waves. That started the era of radio astronomy, which enabled various discoveries like the discovery of pulsars in 1968 [6] by J. Bell. Around the 1950s, the first infrared observations were made for astronomical purposes. Nowadays, infrared astronomy plays an important role in observations of the early universe due to the redshift imposed by its expansion. During that time, the first rocket-borne UV observatories were also launched to start astronomical observations in the UV band. In the 1970s, the first UV satellites were launched to observe for longer periods. In the early 1960s, the first X-ray source Sco X-1 was discovered with a rocket-borne X-ray observatory [7]. The first detection of  $\gamma$ -rays from the galactic plane happened in 1968 with the OSO-3 observatory [8]. Nowadays,  $\gamma$ -ray observations are used to detect gamma-ray bursts and blazars (among others). In multi-wavelength astronomy, all of these wavelength bands are combined.

This approach of combining observations in different wavelengths can be expanded to observing different messengers and combining that information. There are three additional messengers to photons. Cosmic rays are highly energetic, mostly charged particles hitting the Earth's atmosphere from space. They were discovered in 1912 by Victor Hess [9]. The first indirect detection of gravitational waves in 1981 [10] was confirmed by the first direct detection in 2016 [11]. These gravitational waves are produced in merger events of two compact objects like black holes and neutron stars. The last category of messengers is neutrinos. The first extraterrestrial neutrinos were detected in 1968 originating from the sun [12]. In 1987, the first extrasolar neutrinos were observed from the supernova SN1987A in the Large Magellanic Cloud [13]. Both of these sources emit low-energy neutrinos but no high-energy neutrinos. The IceCube Neutrino Observatory discovered a

diffuse astrophysical flux of high-energy neutrinos in 2013 [14] and in 2023 they discovered a significant neutrino signal from our own galaxy [15] in the IceCube data. There are individual point source candidates as the Seyfert Galaxy NGC 1068 [16] and the blazar TXS 0506+056 [17].

Every messenger has advantages and disadvantages for certain types of observations. We have a lot of experience in photon observations. That enables observations of numerous objects across the universe. However, there are physical limitations in observing the universe through photons as they get absorbed by matter depending on their energy. Also, the maximum distance of photons in general that can reach us is limited by the cosmic microwave background (CMB) and the extragalactic background light (EBL). Therefore, the first  $\sim 10^5$  years of the universe can not be studied using photons as messengers since the universe was not transparent for them before that time. With other messengers, in principle, one can look back further in time. The neutrino cosmic horizon originates at the epoch of their last scattering, about 0.1 s after the Big Bang [18], which marks the theoretical limit in distance for neutrino observations. The theoretical limit of gravitational wave observations is around the Planck time  $10^{-43}$  s. At these distances, one could observe gravitational waves from the Big Bang itself [18]. Therefore, if those early neutrinos or gravitational waves could be detected, it would open a new window into the early universe. These observations are outside of the current experimental reach. Besides the very early universe, each messenger provides a unique point of view on astronomical objects that can be suitable for the detection of characteristic mechanisms. For example, since we observe highly energetic cosmic rays, there must be some acceleration mechanism able to reach the observed energy. Neutrinos are a smoking gun for hadronic processes in the universe. Therefore, the combination of multiple messengers can be very beneficial. This approach is called multi-messenger astronomy.

This thesis is focused on neutrino astronomy. The aim is to study the performance of IceCubePy, a python-based software under development that uses an unbinned likelihood approach to search for point sources in the 10-year public data set of the IceCube Neutrino Observatory<sup>1</sup> [19] containing only track events. This work presents the performance of the IceCubePy v0.28.1 version. In chapter 1, I introduce cosmic rays in more detail and their connection to neutrino astronomy. After that, I describe cosmic neutrinos and their potential production mechanism in astrophysical sources. I also show potential source candidates for astrophysical neutrinos. I will go into more detail about Active Galactic Nuclei (AGN). In chapter 2, I describe the IceCube Neutrino Observatory, its detection

---

<sup>1</sup><https://icecube.wisc.edu/data-releases/2021/01/all-sky-point-source-icecube-data-years-2008-2018/>

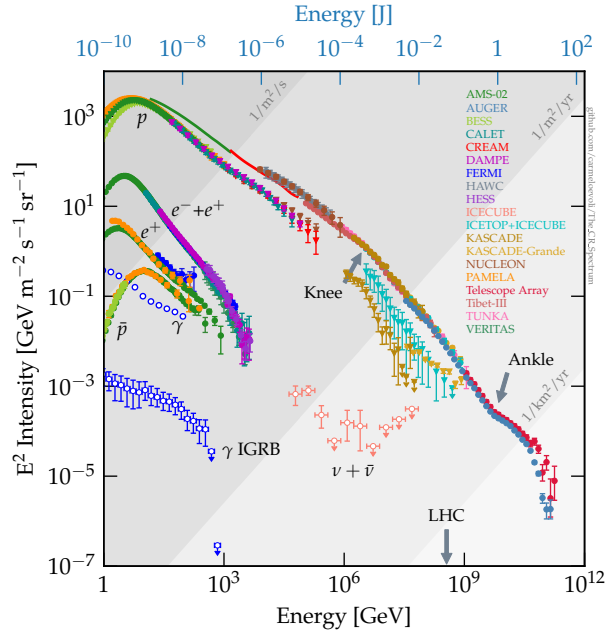


**Figure 1.1:** Differential spectrum of cosmic rays as a function of energy. The spectrum follows a power law with minor deviations. The gray bands show the rate at which cosmic rays hit the Earth’s atmosphere. Figure taken from [20].

mechanism and the 10-year public dataset of track events. The unbinned likelihood approach for the point-source search is presented in chapter 3. In chapter 4, I present and discuss the results of my performance study. I calculated the sensitivity, the  $3\sigma$  and the  $5\sigma$  discovery potential flux (section 4.1) and analyzed the fit bias of the parameters that are optimized in the maximum likelihood analysis (section 4.2). In the end, a brief outlook will be given on the future perspectives of the IceCubePy software and the unbinned likelihood analysis for the point source search in IceCube data.

## 1.1 Cosmic Rays

Cosmic rays consist of 90% protons, followed by ionized helium and other ionized heavier elements. The cosmic ray spectrum covers several orders of magnitude in energy, starting from GeV energies up to  $\sim 100$  EeV. The spectrum is shown in fig. 1.1. The spectrum follows a power law with a best-fit spectral index of 2.7 [21] up to PeV energies. There, the spectrum softens, a feature called *the knee*. At EeV energies, the spectrum re-hardens, a feature called *the ankle*.

Charged particles can be accelerated by Fermi shock acceleration by scattering at shock fronts, leading to a spectrum following an unbroken power law  $\propto E^{-2}$  at the production site. Due to diffusion phenomena in the Milky Way, a source spectrum with spectral index 2 is observed as  $\propto E^{-2.6}$ . That is compatible with the observed cosmic ray spectrum [21].

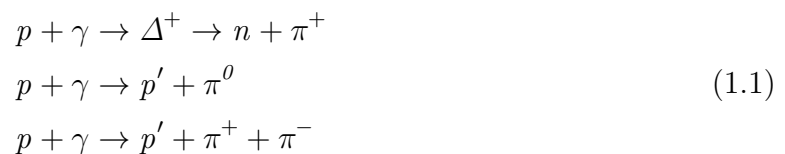
Since cosmic rays are charged, they are deflected by magnetic fields. Galaxies have magnetic fields but there are also magnetic fields in the intergalactic space. Therefore, it is very difficult to point to the sources of the cosmic rays from their very anisotropic flux and the sources of cosmic rays are still not confirmed. Finding the sources of cosmic neutrinos could help because highly energetic neutrinos need hadronic processes that would also be able to produce cosmic rays. That makes astrophysical neutrinos a good tracer for the origin of cosmic rays.

## 1.2 Neutrinos

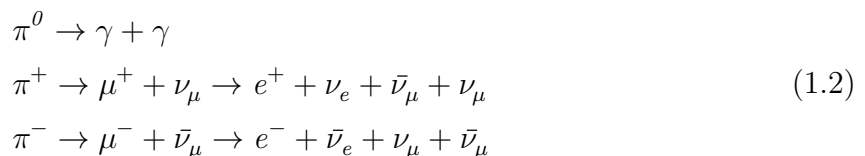
Neutrinos are neutral elementary particles with a small but non-zero mass. They are fermions belonging to the lepton category and exist in three flavors: *electron neutrino*  $\nu_e$ , *muon neutrino*  $\nu_\mu$  and *tau neutrino*  $\nu_\tau$ . Since they are leptons, they do not interact via strong interaction and being electrically neutral, they also do not interact via electromagnetic interaction. Because of their very small mass ( $m_\nu \ll 1 \text{ eV}$ ), gravity is considered negligible. For experimental purposes, neutrinos only interact via weak interaction.

Since neutrinos are not charged, they are not deflected by magnetic fields. Hadronic processes are fundamental in the production of neutrinos at high energies. These highly energetic neutrinos are produced when interacting hadrons produce pions. When charged pions decay, neutrinos are produced. Therefore, astrophysical neutrinos are a smoking gun for hadronic processes in astrophysical objects.

In **proton-photon ( $p\gamma$ ) processes**, a proton interacts with a photon. In an AGN jet, the relativistic protons can interact with low-energy photons that are either internally produced by the AGN itself or externally [22] (more details on AGN in section 1.3.1). There are three main channels, with the resonant production of a  $\Delta^+$  hadron being the dominant process:



The neutrinos are produced in the decay of charged pions (branching ratio  $\sim 100\%$ )



Ignoring the distinction between neutrinos and anti-neutrinos, the pion decay leads to a neutrino flavor ratio of 1 : 2 : 0 in the flavor order  $\nu_e, \nu_\mu, \nu_\tau$ . In the delta resonance channel, the  $\pi^+$  has  $\sim 20\%$  of the proton's energy. Since the pion decays into four particles and the pion mass is significantly larger than all decay product masses ( $m_{\pi^+} \gg m_e, m_\nu$ ), the pion energy is distributed evenly across the decay products. Therefore, the outgoing neutrino has 5% of the proton's energy [23]:

$$E_\nu \sim 0.05 E_p. \quad (1.3)$$

In the  $p\gamma$  process, both charged and neutral pions are produced. Since neutral pions decay into two photons and charged pions produce neutrinos during their decay, highly energetic neutrinos are connected to highly energetic photons. One needs to take into account, that highly energetic photons can be produced in multiple mechanisms. Also, the photons can be absorbed either at the production site itself or on their path towards the Earth. So  $\gamma$ -rays sources are interesting candidates to search for neutrino emission at their position.

In **proton-proton ( $pp$ ) processes**, a relativistic proton interacts with a low-energy target proton. In these interactions, pions are generated

$$\begin{aligned} p + p &\rightarrow \pi^0 + X \\ p + p &\rightarrow \pi^+ + \pi^- + Y, \end{aligned} \quad (1.4)$$

with  $X$  and  $Y$  being hadronic states. Decaying pions produce neutrinos and photons according to eq. (1.2). The spectrum of neutrinos produced via  $pp$  processes follows the spectrum of the cosmic rays at the production site, therefore the neutrinos spectrum follows a power law spectrum  $\propto E^{-2}$  [21].

### 1.3 Candidate Sources

Despite observations for over ten years, there are only a few point source candidates with high significance detected. Combining them with the galactic emission, they can not explain the diffuse astrophysical flux observed by IceCube. The proposed production mechanisms presented above can take place in several astrophysical objects. Two examples of potential sources for a steady neutrino flux are AGN and supernova remnants. Transient phenomena like gamma-ray bursts are possibly related to transient neutrino emission. Since NGC 1068 and TXS 0506+056, the point source candidates with the highest level of confidence (a global significance of  $4.2\sigma$  and  $3\sigma$ , respectively) [16, 17] are classified as AGN, I will go into more detail on AGN as potential neutrino sources.

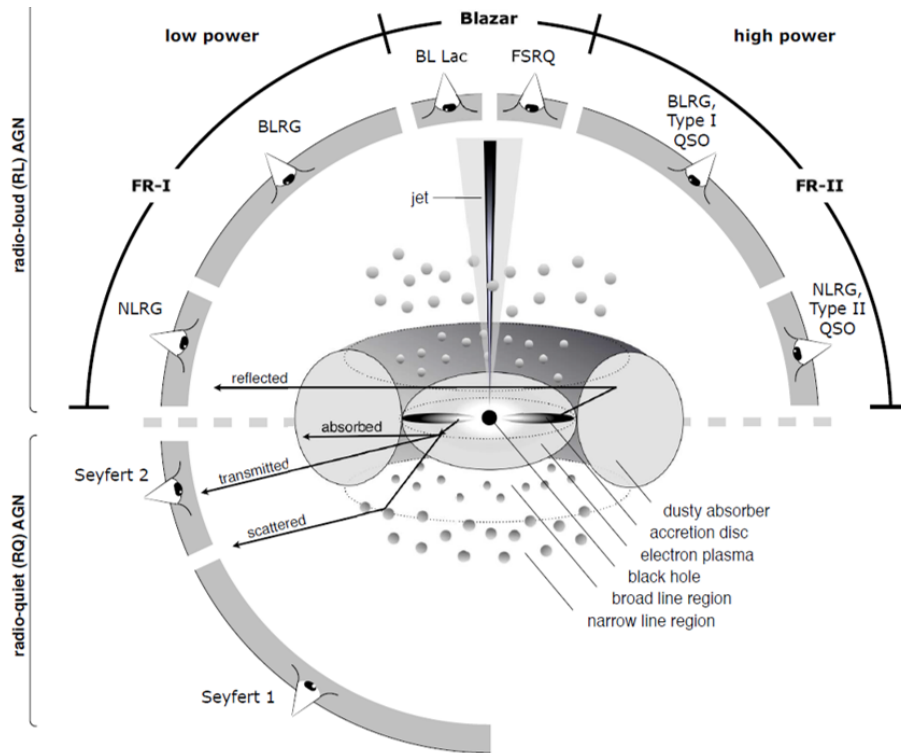


**Figure 1.2:** Schematic representation of possible AGN classifications, figure from [24]. The central supermassive black hole and its accretion disk are surrounded by a dusty torus, the broad line region and the narrow line region. AGN are classified based on their orientation with respect to the observer’s line of sight.

### 1.3.1 Active Galactic Nuclei

It is assumed that all galaxies host a *Supermassive Black Hole* (SMBH) with a mass of  $10^6 M_{\odot}$  to  $10^{10} M_{\odot}$  in their center. A small fraction of these galaxies emit electromagnetic radiation with a high bolometric luminosity across the electromagnetic spectrum additionally to the luminosity produced by stars. This radiation originates from the central region of these galaxies and is powered by mass accretion into the SMBH. These central regions are called *Active Galactic Nuclei* (AGN). The SMBH is surrounded by an accretion disk and a dusty torus. Above and below the plane of the accretion disk and the dusty torus, there is the broad line region (BLR) near the plane and the narrow line region (NLR) more distant from the plane. In some cases, AGN also emit material outflows and collimated relativistic jets perpendicular to the accretion disk.

The matter accreting into the SMBH forms a disk through accretion and heats up. The BLR and NLR consist of clouds that get ionized by the thermal emission of the disk. They then re-emit emission lines which are broadened by the rotation of the system. Since the BLR is closer to the rotating SMBH, its lines are broadened significantly by the Doppler effect, whereas the NLR is much more distant and therefore emits narrow

lines. Depending on the inclination of the AGN with respect to the observer, the dusty torus can block the view toward the BLR and the disk. The relativistic jet can be formed due to the rotation of magnetic fields in the accretion disk, but the exact jet launching mechanism is not confirmed yet.

Based on the presence of a relativistic jet, two major categories of AGN are defined as shown in fig. 1.2: Jetted AGN have a high emission in radio frequencies from electron synchrotron radiation occurring in the jet and are called *radio-loud AGN*. Active galactic nuclei without a relativistic jet are called *radio-quiet AGN*. A more refined classification of AGN is based on the AGN's inclination with respect to the line of sight of the observer and spectroscopic properties and is described in detail by Padovani et al. (2017) in [25]. A jetted AGN that is observed face-on, meaning the jet is aligned with the observer's line of sight, is categorized as a blazar. Traditionally, blazars are subdivided based on the presence of emission lines in their optical spectrum. A blazar with a flat optical spectrum with observable emission lines is categorized as a flat-spectrum radio quasar. When no emission lines can be observed, the blazar is classified as a BL Lacertae (BL Lac) object. However, recent work indicates that this division might not be based on physical differences between the types. It rather suggests dividing blazars based on their radiation efficiency [26, 27, 28].

In relativistic jets, particles get accelerated to relativistic energies and emit photons and, through hadronic processes, also cosmic rays and neutrinos [22]. When the jet is aligned with the observer's line of sight, the observed energies get boosted and the emission is collimated due to relativistic effects.

## Chapter 2

# IceCube Neutrino Observatory

The *IceCube Neutrino Observatory* [29] is a neutrino detector located in Antarctica at the geographical South Pole. The goal of this experiment is to detect high-energy astrophysical neutrinos in the range between TeV and PeV energies [29], using  $1 \text{ km}^3$  of antarctic ice as a detection volume. IceCube detects the Cherenkov radiation induced by secondary charged particles that are produced in an interaction of a neutrino with the surrounding environment (ice and Earth's crust). Therefore, the detector medium has to be transparent for optical photons. To fulfill this criterion, the detector volume is between 1.45 km and 2.45 km below the surface where the ice is transparent [21]. Additionally, the ice above the detector acts as a shield for atmospheric muons (see section 2.4).

When a high-energy neutrino interacts with a nucleon in the ice, charged particles are produced. Due to the high energy of the incoming neutrino, the velocity of the charged particles  $v$  is larger than the reduced speed of light in the ice  $v > \frac{c}{n}$  with  $c$  being the speed of light in vacuum and  $n$  being the refractive index of the detector material. This causes the emission of Cherenkov radiation consisting of blue light emitted in a cone with the particle's trajectory as its axis. To detect the Cherenkov radiation, the volume is instrumented with a three-dimensional array of a total of 5160 *Digital Optical Modules* (DOMs) containing each one photomultiplier tube. The DOMs are mounted on 86 support and read-out cables, forming so-called strings. The vertical spacing between two DOMs on the same string is 17 m, therefore, one string of the length of 1 km holds 60 DOMs. The spatial distribution of the strings follows a hexagonal grid with a horizontal spacing of 125 m (see Fig. 2.1). In the center of the detector, the density of the DOMs is increased to reduce the energy threshold to  $\sim 10 \text{ GeV}$ . This central region is called *DeepCore* [29].



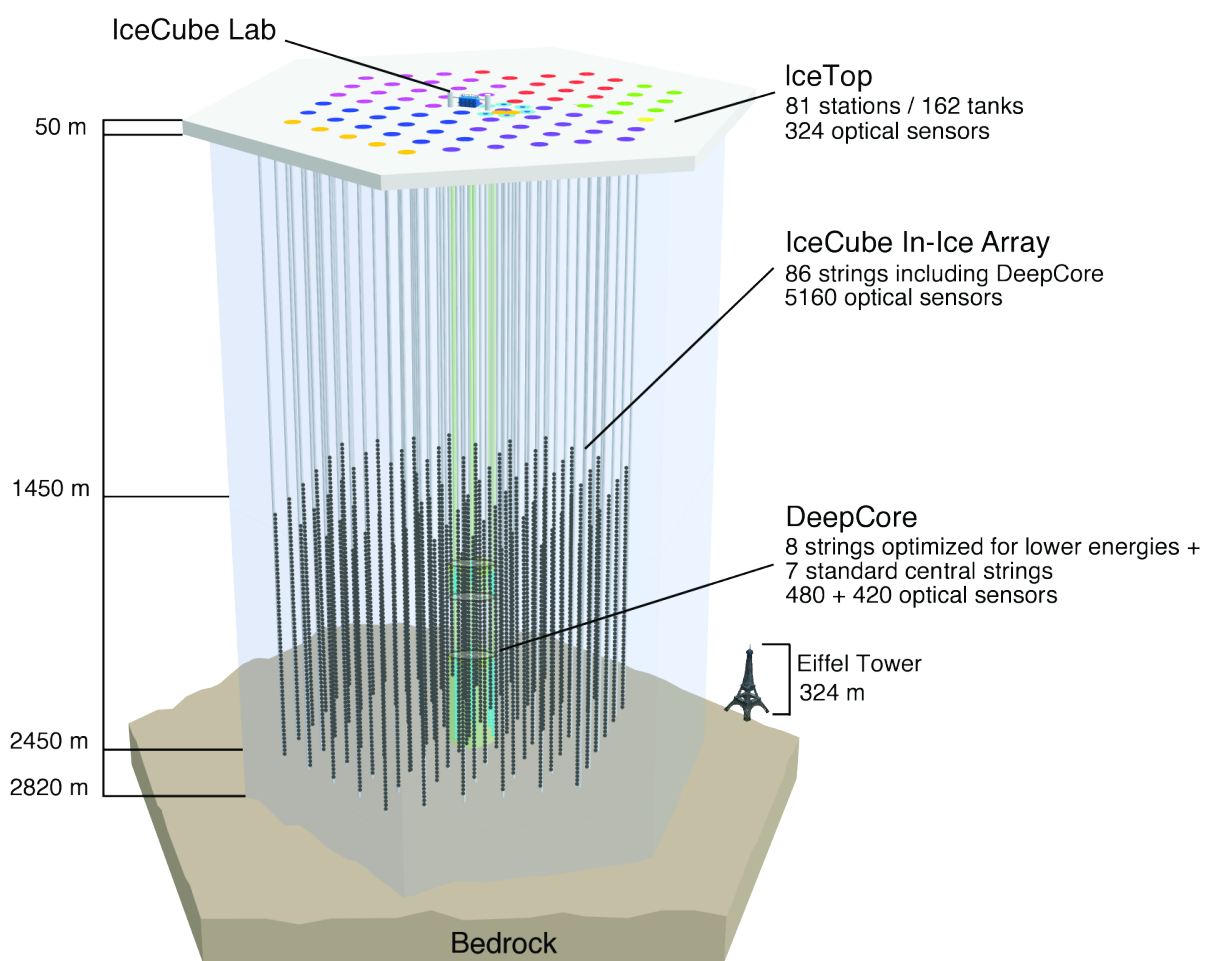


**Figure 2.1:** IceCube Neutrino Observatory setup [29]

## 2.1 Detection Interactions

As explained in section 1.2, all three neutrino flavors only interact significantly via the weak interaction. To detect a neutrino in the IceCube detector, there are two possible interactions:

1. **Neutral-Current interaction (NC)** is the interaction of a neutrino with a nucleon  $X$  of the detector medium via the  $Z^0$  boson. In this interaction, the incoming neutrino exchanges energy with  $X$  so that the outgoing neutrino remains unchanged except for the energy. The nucleon  $X$  is fragmented, forming hadrons from quark, anti-quark pairs and causing a hadronic cascade  $Y$ . This interaction can happen for each neutrino flavor  $l = \{e, \mu, \tau\}$ :

$$\nu_l + X \xrightarrow{Z^0} \nu_l + Y \quad (2.1)$$

2. **Charged-Current interaction (CC)** is the interaction of a neutrino with a nucleon  $X$  via the  $W^\pm$  boson. Here, the incoming neutrino is converted into the charged lepton of its flavor. Similar to NC interactions, the nucleon can cause a hadronic cascade  $Y$  due to fragmentation:

$$\nu_l + X \xrightarrow{W^\pm} l^\pm + Y \quad (2.2)$$

If the energy of an outgoing particle is sufficient, it will cause a chain of secondary particle production, called a shower or cascade. Two types of showers are relevant to the IceCube detector:

1. **Electromagnetic shower:** This type of shower is triggered by photons, electrons, or positrons, but never by hadrons. A high energy photon ( $E > 1 \text{ MeV}$ ) can interact with the detection medium  $X$  via pair production:

$$\gamma + X \rightarrow e^- + e^+ + X \quad (2.3)$$

High-energy electrons or positrons can interact with the detection medium via bremsstrahlung:

$$e^\pm + X \rightarrow e^\pm + \gamma + X \quad (2.4)$$

The photon from this interaction can produce another  $e^+/e^-$  pair if the energy is sufficient. These two processes produce the starting particles of the other process respectively. Therefore, they can form a chain of alternating reactions. The shower stops when all outgoing particles do not have enough energy to trigger the next reaction in the chain.

2. **Hadronic shower:** A hadronic shower is triggered by the interactions of hadrons with matter. Those interactions produce pions ( $\pi^0, \pi^\pm$ ) among other products. The  $\pi^0$  meson decays within  $8.43 \times 10^{-17}$  s (in its rest frame) into two photons in 98.823 % of the cases [30]. Due to relativistic effects, they have a longer lifetime. Therefore, depending on their energy, some  $\pi^0$  mesons can interact with the medium before decaying. These photons each produce an electromagnetic shower. The  $\pi^\pm$  mesons decay slower, their mean lifetime in their rest frame is  $2.6033 \times 10^{-8}$  s. Before their decay, they can trigger other hadronic interactions with the detector medium producing additional  $\pi^0$  and  $\pi^\pm$ . The  $\pi^\pm$  decays as described in eq. (1.2). These hadronic processes can also form a chain of reactions creating a hadronic shower. The hadronic shower stops when all outgoing particles do not have enough energy to trigger the next reaction.

## 2.2 Event Morphology

In the IceCube detector, three different event morphologies can be observed [21].

- **Cascade events:** In NC interactions of all neutrino flavors, the hadronic fragments cause a hadronic shower. In CC interactions of the electron neutrinos, the outgoing electron starts an electromagnetic shower. The hadronic fragments also contribute to the event with a hadronic shower. The particles in the showers can induce Cherenkov radiation that is detected by the DOMs. This event has a roughly spherical morphology, as shown in figure 2.2 in the middle figure. The advantage of this type is it allows for high energy resolution because the neutrino energy is fully deposited in the detection medium. However, the downside is the low angular resolution ( $\sim 10^\circ - 15^\circ$  [2]) because the particles are highly scattered and the emission is not concentrated around a single axis.
- **Track events:** When muon neutrinos interact via CC interaction, they are converted into muons. These muons are relativistic and emit Cherenkov radiation. They do not scatter significantly in the detector medium, so it produces a straight track signal (see fig. 2.2 right figure). The angular distance between the reconstructed muon direction and the true neutrino direction is described by the *Point Spread Function* (PSF). Generally, it decreases with increasing energy [19]. This leads to a good angular resolution of typically  $\lesssim 1^\circ$  for energies above the TeV range [2]. Since the muon does not scatter in the ice, it leaves the detector volume after depositing only a fraction of its energy. Therefore, the energy resolution is worse than in cascade events.

- Double bang events:** When tau neutrinos interact via CC interaction, they are converted into tau leptons. At the neutrino vertex, a hadronic shower caused by the hadronic fragments  $Y$  produces a spherical signal. The  $\tau$ -lepton leaves this vertex without scattering. Due to its short lifetime of  $2.903 \times 10^{-13}$  s (rest frame) [30], it decays near the neutrino vertex (see fig. 2.2 left figure). Depending on their energy, due to relativistic time dilation tau neutrinos can travel a distance long enough before their decay to be distinguishable from cascade events. The branching ratio for the  $\tau$ -lepton decaying into hadrons is  $\sim 64.79\%$ , for a decay into  $\nu_\tau e \nu_e$  it is  $17.82\%$  and for a decay into  $\nu_\tau \mu \nu_\mu$  it is  $17.39\%$  [30]. The hadronic decay and the decay into an electron cause another cascade signal at the decay vertex. If the  $\tau$ -lepton decays into a muon, the muon leaves the detector on a straight path.

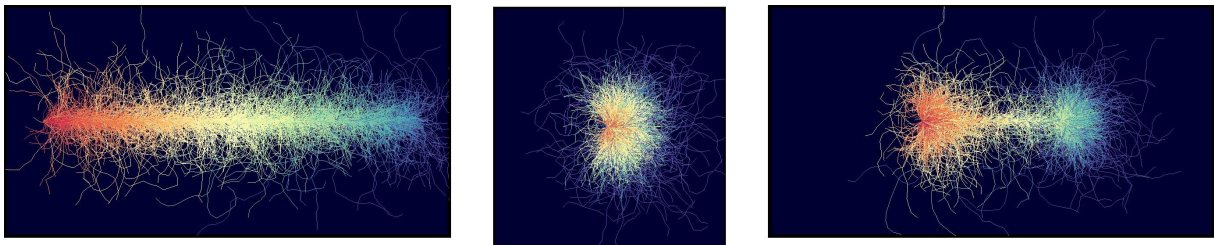


**Figure 2.2:** A simulation of the propagation of Cherenkov light in the detector in all three event topologies: a track event (left), a cascade event (middle), and a double bang event (right). The relative detection time is encoded in the color. Red photons are early, blue ones are detected late. (Figure taken from [31])

NC interactions do not distinguish between neutrinos and anti-neutrinos. For CC interactions, the only difference is the charge of the outgoing lepton. Since the signal does not carry information about the charge, IceCube can not distinguish between neutrinos and anti-neutrinos. From now on, we will make no distinction between neutrinos and anti-neutrinos.

## 2.3 IceCube 10-Year Dataset

The IceCube Collaboration released a sample of 1 134 450 track events observed in the years from 2008 to 2018 [19]. The dataset is divided into ten seasons, each about one year long. In table 2.1 the seasons are listed together with the number of events in the dataset. In the first three seasons, only 40, 59, and 79 strings were deployed respectively. Only in the latest seven seasons, all 86 strings were installed. Each season label uses the prefix "IC", followed by the number of installed strings and Roman Numerals I-VII for the seasons with all 86 strings installed. The following work uses this dataset.

Season	Events
IC40	36900
IC59	107011
IC79	93133
IC86-I	136244
IC86-II	112858
IC86-III	122541
IC86-IV	127054
IC86-V	129311
IC86-VI	123657
IC86-VII	145750

**Table 2.1:** List of the IceCube seasons with the corresponding number of events in the 10-year dataset.

To study the detector’s response to track events coming from astrophysical neutrinos, the IceCube collaboration performed Monte Carlo simulations. These simulations studied the effective area  $A_{\text{eff}}$  that changes with the declination and the neutrino energy. They also studied the *Point Spread Function* (PSF) which describes the angular distance between the true neutrino direction and the reconstructed muon direction. Additionally, the energy reconstruction was studied. The reconstructed quantities are used as input for the *Probability Density Functions* (PDF) used in the maximum likelihood analysis (see chapter 3) [19].

The data release contains the detected events characterized by

- event arrival time in Modified Julian Date (MJD) with a millisecond precision
- reconstructed energy of a muon passing through the detector in  $\log\left(\frac{E}{\text{GeV}}\right)$
- reconstructed origin of the particle given in local detector coordinates (azimuth and zenith in degrees) and equatorial coordinates (declination and right ascension in degrees)
- estimated angular uncertainty of the reconstructed direction in degrees. The uncertainty is assumed to be symmetric in azimuth and zenith. An uncertainty floor of  $0.2^\circ$  is applied.

In addition to the events, the IceCube Collaboration published

- a ‘good run list’, a list of time intervals where the data taken is useful for scientific analysis.

- *instrument response functions* (IRF): The response of the IceCube detector to simulated neutrinos for different configurations depending on the neutrino energy and declination. The IRF is calculated using Monte Carlo simulations and is published in 3 spatial bins:  $\delta < -10^\circ$ ,  $-10^\circ < \delta < 10^\circ$  and  $\delta > 10^\circ$ .
- *effective areas*: The effective area of the detector that is needed to calculate the expected event rate in the detector from a given flux assumption.

## 2.4 Atmospheric Background

Cosmic rays hitting the atmosphere trigger a cascade of secondary particle production analog to the cascades described in section 2.1. Among other particles, muons and neutrinos are produced. The atmospheric muons are shielded by the Earth, meaning they can only reach the detector for zenith angles  $\lesssim 90^\circ$ . Because of their instability, they decay during their path through the atmosphere. Therefore, the abundance of atmospheric muons decreases with the zenith angle. Because of the location of the IceCube Neutrino Observatory at the geographic South Pole, its zenith angle can be easily converted to the declination (a zenith angle of  $0^\circ$  corresponds to a declination angle of  $-90^\circ$ ). The atmospheric muons contribute significantly to the atmospheric background only for declinations  $\delta < -5^\circ$ . This marks the boundary between the southern hemisphere ( $\delta < -5^\circ$ ) and the northern hemisphere ( $\delta \geq -5^\circ$ ) [19]. The transmission probability of neutrinos through the Earth depends on the zenith angle and the particle's energy. The transmission probability of neutrinos with respect to the IceCube position is shown in fig. 2.3. Since the atmospheric background follows a soft power law with a spectral index of  $\gamma = 3.7$  [21], a high percentage of atmospheric neutrinos do not reach very high energies which would lead to absorption by the Earth. Atmospheric events (muons and neutrinos) dominate the data measured by IceCube. To reduce the background different filters are applied in the event selection. This leads to different energy cuts in the 10-year dataset for the two hemispheres. In the southern hemisphere, the data is cut below a minimum energy depending on the declination. This is shown in fig. 2.4 (left).

Due to the location of the IceCube observatory near the geographical South Pole, the data appears uniform in right ascension on time scales  $> 24$  h. This uniformity is caused by the Earth's rotation. When integrating over several days, the background becomes uniform for all right ascension. In declination, a clear variation can be seen (see fig. 2.4 (right)). In the southern hemisphere, there are less events than in the northern hemisphere due to the hard energy cut applied to the data to reduce atmospheric muons. In the northern hemisphere, the number of events decreases with increasing declination due to the increasing absorption in the Earth.

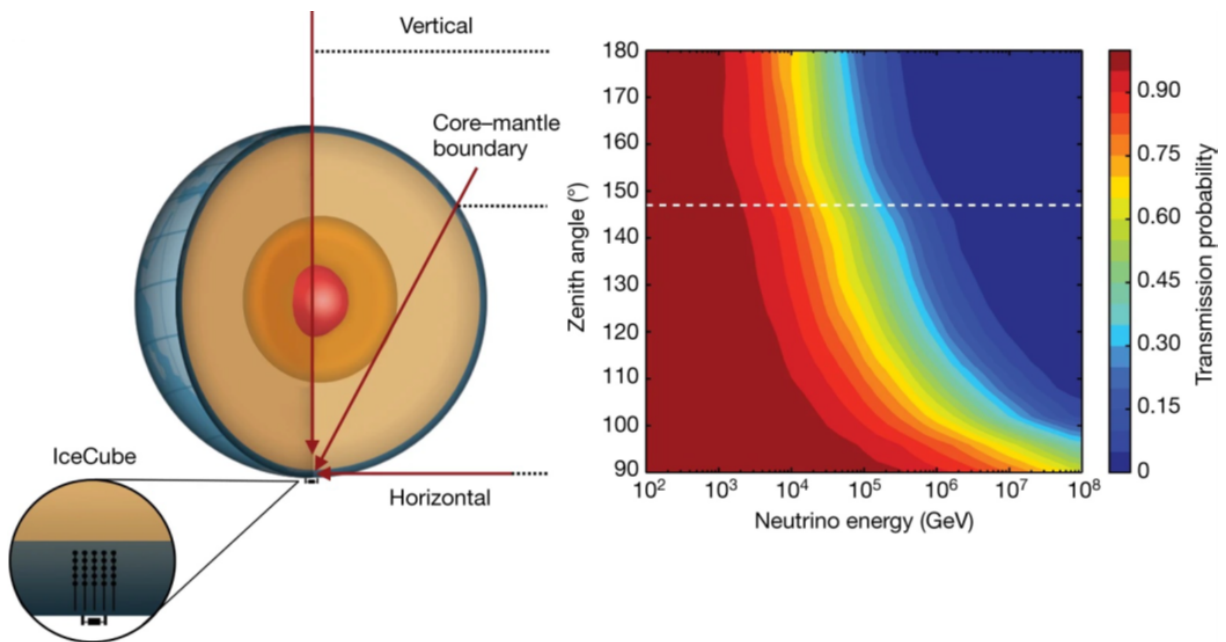


**Figure 2.3:** (left) Scheme of the position of IceCube on earth with the definition of the zenith angle measured from the zenith of IceCube. (right) Transmission probability of neutrinos through Earth depending on their energy and zenith angle (standard model prediction). The white dotted line marks the core-mantle boundary. (Figure taken from [32])

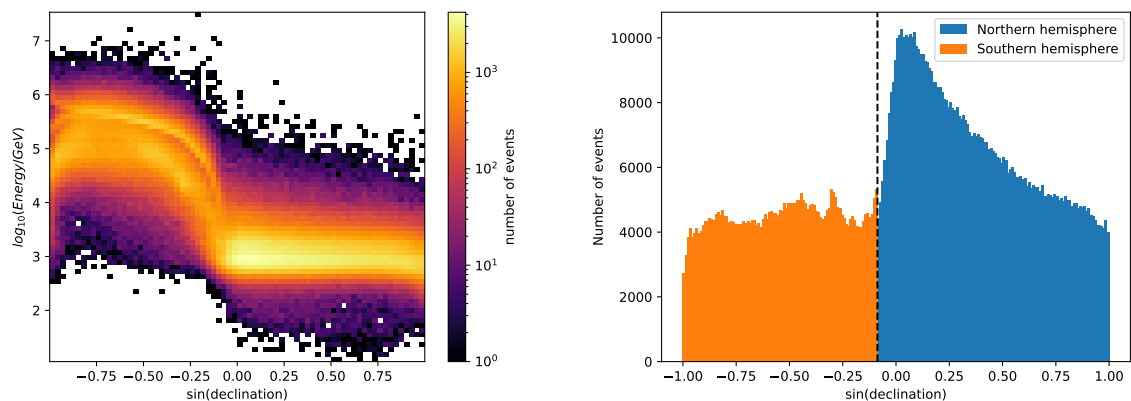


**Figure 2.4:** Properties of the 10-year public dataset. (left) Energy distribution depending on the declination. (right) Number of events depending on the declination.

## Chapter 3

# Statistical Methods

### 3.1 Unbinned Likelihood Ratio Test

This section is mainly based on [21]. The likelihood function  $\mathcal{L}(\mathbf{x}|\boldsymbol{\theta})$  is the probability of observing the data  $\mathbf{x}$  when assuming a model described by a set of parameters  $\boldsymbol{\theta}$ . In this function, the observed data  $\mathbf{x}$  is fixed and the model  $\boldsymbol{\theta}$  is a variable. The goal is to find the best model that describes the observed data. The probability density function (PDF)  $f(x_i|\boldsymbol{\theta})$  defines the probability that a data point has the value  $x_i$  when a set of parameters  $\boldsymbol{\theta}$  is given. The likelihood function is defined as

$$\mathcal{L}(\mathbf{x}|\boldsymbol{\theta}) = f(\mathbf{x}|\boldsymbol{\theta}) = \prod_i f(x_i|\boldsymbol{\theta}). \quad (3.1)$$

A likelihood ratio test is a hypothesis test. A hypothesis test compares two dichotomous hypotheses, the null hypothesis  $H_0 : \boldsymbol{\theta} \in \Theta_0$  and the alternative hypothesis  $H_1 : \boldsymbol{\theta} \in \Theta_0^C$ , with  $\Theta_0$  being a subset of the parameter space and  $\Theta_0^C$  being its complement. The hypothesis test tries to answer whether to accept  $H_0$  as true or reject  $H_0$  and accept  $H_1$ . [33]

In the following analysis, I use an unbinned likelihood ratio test for point sources in the dataset. The hypotheses for this test are formulated as follows:

- **Background hypothesis**  $H_0 : \boldsymbol{\theta} = \boldsymbol{\theta}_0$ : The neutrino flux is produced by atmospheric muon and neutrino events and diffuse astrophysical neutrinos.
- **Signal hypothesis**  $H_1 : \boldsymbol{\theta} = \boldsymbol{\theta}_1$ : The neutrino flux has a signal component in addition to the background events. This signal consists of neutrino events clustered around the source position  $\mathbf{x}_S = (\alpha_S, \delta_S)$ . The point source has an unbroken power law emission spectrum  $\frac{d\phi}{dE_\nu} \propto E_\nu^{-\gamma}$ .



The number of detected neutrinos  $N$  follows a Poisson distribution with an expected number of events  $\lambda$ :

$$P(N|\lambda) = \frac{1}{N!} \lambda^N \exp(-\lambda) \quad (3.2)$$

Since the order of the events can be neglected, the factor of  $1/N!$  can be omitted. To take the Poisson distribution into account, the likelihood function is extended by the Poisson distribution. This is called an extended likelihood.

$$\begin{aligned} \mathcal{L}(\mathbf{x}|\boldsymbol{\theta}) &= P(N|\lambda) \cdot \prod_i^N f(\mathbf{x}_i|\boldsymbol{\theta}) = e^{-\lambda} \prod_i^N \lambda \cdot f(\mathbf{x}_i|\boldsymbol{\theta}) \\ &= e^{-\lambda} \prod_i^N P(\mathbf{x}_i|\boldsymbol{\theta}) \end{aligned} \quad (3.3)$$

$P(\mathbf{x}_i|\boldsymbol{\theta})$  is the PDF normalized to  $\lambda$ .

The dataset contains  $n_S$  signal events and  $n_B$  background events, which add up to the total number of events  $N = n_S + n_B$ . Since the probability of one single event being a signal event  $S(\mathbf{x}_i|\boldsymbol{\theta})$  differs from the probability of being a background event  $B(\mathbf{x}_i)$ , the probability  $P(\mathbf{x}_i|\boldsymbol{\theta})$  to observe an event is a combination of these two probabilities:

$$P(\mathbf{x}_i|\boldsymbol{\theta}) = \frac{n_S}{n_S + n_B} S(\mathbf{x}_i|\boldsymbol{\theta}) + \frac{n_B}{n_S + n_B} B(\mathbf{x}_i). \quad (3.4)$$

When approximating the expected number of events with the observed number of neutrinos  $\lambda \rightarrow n_S + n_B = N$ , the likelihood function is defined as follows:

$$\mathcal{L}(\mathbf{x}|\boldsymbol{\theta}) = e^{-N} \prod_i^N \left[ \frac{n_S}{N} S(\mathbf{x}_i|\boldsymbol{\theta}) + \left(1 - \frac{n_S}{N}\right) B(\mathbf{x}_i) \right] \quad (3.5)$$

To test whether the background hypothesis  $H_0$  or the signal hypothesis  $H_1$  is the preferred description of an event, the unbinned likelihood test is used. To compare the two hypotheses, the likelihood ratio is defined as

$$\lambda(x) = \frac{\sup_{\boldsymbol{\theta}_0} \mathcal{L}(\mathbf{x}|\boldsymbol{\theta})}{\sup_{\boldsymbol{\theta}_1} \mathcal{L}(\mathbf{x}|\boldsymbol{\theta})} = \frac{\mathcal{L}(\mathbf{x}|\boldsymbol{\theta}_0)}{\mathcal{L}(\mathbf{x}|\boldsymbol{\theta}_1)}. \quad (3.6)$$

The likelihood ratio  $\lambda(x)$  can be simplified since the likelihood function at the maximum likelihood estimator in the parameter space can replace the supremum of the likelihood function over the parameter space. The background hypothesis is rejected for  $\lambda(x) < k$ ,  $k$  being a critical value depending on the required significance level. It is useful to use the log-likelihood test statistic ( $TS$ ) defined as

$$TS = -2 \ln \lambda(x) = 2 \ln \left[ \frac{\mathcal{L}(\mathbf{x}|\boldsymbol{\theta}_1)}{\mathcal{L}(\mathbf{x}|\boldsymbol{\theta}_0)} \right]. \quad (3.7)$$

According to *Wilk's theorem*, the  $TS$ -distribution follows a  $\chi^2$  distribution if the background hypothesis  $H_0$  is true. It is expected that the  $\chi^2$  distribution has between 1 and 2 degrees of freedom because the two variables  $n_S$  and  $\gamma$  are not completely independent. When plugging the likelihood function eq. (3.5) in, the test statistics is defined as

$$\begin{aligned} TS &= 2 \ln \left[ \frac{\mathcal{L}(\mathbf{x}|\boldsymbol{\theta}_1)}{\mathcal{L}(\mathbf{x}|\boldsymbol{\theta}_0)} \right] = 2 \ln \left[ \frac{\mathcal{L}(\hat{n}_S, \hat{\gamma})}{\mathcal{L}(n_S = 0)} \right] \\ &= 2 \sum_i \ln \left[ \frac{\hat{n}_S}{N} \left( \frac{S_i}{B_i} - 1 \right) + 1 \right]. \end{aligned} \quad (3.8)$$

Here, the signal hypothesis describes a point source emitting  $\hat{n}_S$  neutrinos with an emission spectrum with spectral index  $\hat{\gamma}$ . The maximum likelihood approach aims to find the optimal model maximizing the  $TS$  value by varying the number of signal neutrinos  $n_S$  and the spectral index  $\gamma$ . The hat marks the values for  $n_S$  and  $\gamma$  that maximize the  $TS$  value.

## 3.2 Signal and Background PDF

To compare the background hypothesis  $H_0$  and the signal hypothesis  $H_1$ , the PDFs need to be defined for both cases, which depend on the probability of a neutrino being a signal neutrino  $S_i$  or a background neutrino  $B_i$ . As model parameters  $\boldsymbol{\theta}$  for the PDFs we take into account the position of the source  $\mathbf{x}_S = (\alpha_S, \delta_S)$  and the spectral index of the source  $\gamma$ . The data  $\mathbf{x}$  are described by the reconstructed position  $\mathbf{x}_i = (\alpha_i, \delta_i)$ , the uncertainty of the spatial reconstruction  $\sigma_i$  and the reconstructed energy  $E_i$ .

Signal events are expected to be clustered around the position of the potential astrophysical source  $\mathbf{x}_S$ . Its energy spectrum is expected to follow an unbroken power law  $\propto E^{-\gamma}$  with a different spectral index  $\gamma$  than the background expectation. As mentioned in section 1.2, the spectral index of the signal events is expected to be harder than the background index. The signal PDF  $S_i$  can be described by the product of a spatial term and an energy term:

$$\begin{aligned} S_i(\mathbf{x}_i, \sigma_i, E_i | \mathbf{x}_S, \gamma) &= S_{spatial}(\mathbf{x}_i, \sigma_i | \mathbf{x}_S) \cdot S_{energy}(E_i | \delta_i, \gamma) \\ &= \frac{1}{2\pi\sigma_i^2} \exp \left[ -\frac{|\mathbf{x}_i - \mathbf{x}_S|^2}{2\sigma_i^2} \right] \cdot S_{energy}(E_i | \delta_i, \gamma) \end{aligned} \quad (3.9)$$

The spatial PDF term  $S_{spatial}(\mathbf{x}_i, \sigma_i | \mathbf{x}_S)$  is a two-dimensional Gaussian distribution centered at the source position  $\mathbf{x}_S$  with a standard deviation  $\sigma_i$ . The energy PDF term  $S_{energy}(E_i | \delta_i, \gamma)$  is calculated from Monte Carlo simulations based on the effective area of the detector. It describes the probability of observing a signal neutrino with energy  $E_i$

given the declination  $\delta_i$  and the source spectral index  $\gamma$ .

The background PDF  $B_i$  is defined similarly. It represents the background consisting of atmospheric muons, atmospheric neutrinos and astrophysical diffuse neutrino flux. Since background events highly dominate the data, the dataset can be treated as a pure background sample (see section 2.4). Therefore, the background PDF following eq. (3.10) [34] is drawn directly from the dataset. There are no free parameters.

$$\begin{aligned} B_i(\mathbf{x}_i, E_i) &= B_{spatial}(\mathbf{x}_i) \cdot B_{energy}(E_i|\delta_i) \\ &= \frac{1}{2\pi} \frac{N_\nu \in \delta_i \pm [\delta_{min}; \delta_{max}]}{\sin \delta_{max} - \sin \delta_{min}} \cdot B_{energy}(E_i|\delta_i) \end{aligned} \quad (3.10)$$

The spatial PDF term  $B_{spatial}(\mathbf{x}_i)$  is independent of the right ascension  $\alpha_i$  on timescales  $> 24$  h due to the location of the IceCube Neutrino Observatory at the geographic South Pole (see section 2.4). The dependency on the declination is expressed by dividing the sky into stripes in declination that are equally spaced in  $\sin \delta$  and taking the event rate in these stripes. The event rate varies with declination due to the intrinsic declination dependency of the background described in section 2.4 and different selection criteria at different declinations. The energy PDF term  $B_{energy}(E_i|\delta_i)$  describes the probability of observing a background event (neutrino or muon) with a reconstructed energy  $E_i$  at the declination  $\delta_i$ . It can be visualized by building a two-dimensional histogram of the reconstructed energy of the event as a function of the  $\sin \delta_i$  of the event from the 10-year public dataset which is depicted in fig. 2.4.

The signal PDF  $S_i$  and the background PDF  $B_i$  are plugged into eq. (3.8). To find the optimized values for  $n_S$  and  $\gamma$ , both parameters are varied to find the maximum  $TS$  value. A higher  $n_S$  value leads to a higher  $TS$  value.

In this thesis, only the spatial and energy terms of the PDF are covered since this work focuses on steady-state emission. When looking for transient neutrino emission, a temporal PDF term is multiplied as an additional factor to the PDFs.

### 3.3 Sensitivity and Discovery Potential

To define the sensitivity and discovery potential flux one needs to perform pseudo experiments simulating signals. We simulated point sources with different fluxes and performed the pseudo experiment multiple times per flux value with a randomized background realization. These multiple executions of the pseudo experiment for the same simulated point source flux are called trials. The sensitivity flux of an analysis is the source flux for which

in 90 % of the cases the  $TS$  value is higher than the median  $TS$  value of the background. The  $3\sigma$  discovery potential flux of an analysis is the flux, where in 50 % of the cases the  $TS$  value is higher than the  $TS$  value corresponding to a one-tailed p-value equivalent to a  $3\sigma$  Gaussian significance. The p-value can be calculated from a normalized background  $TS$  distribution  $g(TS|H_0)$  with enough trials:

$$p(TS_{obs}) = \int_{TS_{obs}}^{\infty} g(TS|H_0) dTS \quad (3.11)$$

Since the background varies for different declinations, the sensitivity flux and discovery potential flux depend on the declination.

## Chapter 4

# Evaluation of the IceCubePy Performances

Blazars are a promising class of potential neutrino emitters, as described in chapter 1. The *MessMapp* Group studied the relation in a positional cross-correlation study [35] between neutrino hotspots in the southern hemisphere of the 7-year IceCube dataset containing track-like events [36] and the fifth data release of Roma-BZCat catalog [37]. To analyze IceCube data for hotspots and point sources independent of the IceCube collaboration, the *MessMapp* Group currently develops the analysis software `IceCubePy`. `IceCubePy` is written in Python and uses the maximum likelihood method described in sections 3.1 and 3.2 to optimize  $n_S$  and  $\gamma$ . To use this analysis for scientific studies, it is necessary to know how well the fitted parameters align with the true ones and if there are any systematic errors in the fit. To know the true parameters, one simulates point source signals and analyzes them with `IceCubePy`. The signal simulation code is based on a public code developed by Michael Larson<sup>1</sup>. In this thesis, two data samples are simulated:

- A sample of point sources emitting a flux following a power law with spectral index  $\gamma = 2$  ( $\propto E^{-2}$ ) and 100 different neutrino flux values with 100 independent trials each at a fixed declination. This sample is used to study the performance of `IceCubePy` for point sources emitting a hard spectrum.
- A sample of point sources emitting a flux following a power law with spectral index  $\gamma = 3$  ( $\propto E^{-3}$ ) and 100 different neutrino flux values with 100 independent trials each at a fixed declination. Using a spectral index of 3, this sample is used to study the performance for point sources emitting a softer spectrum.

In both samples, the simulations were performed at 21 different declinations that are equally spaced in  $\sin \delta$  for  $\delta \in [-81^\circ, 81^\circ]$ . In the simulations, the 10-year dataset pub-

<sup>1</sup><https://github.com/mjlarson/I3PublicDataSampler>

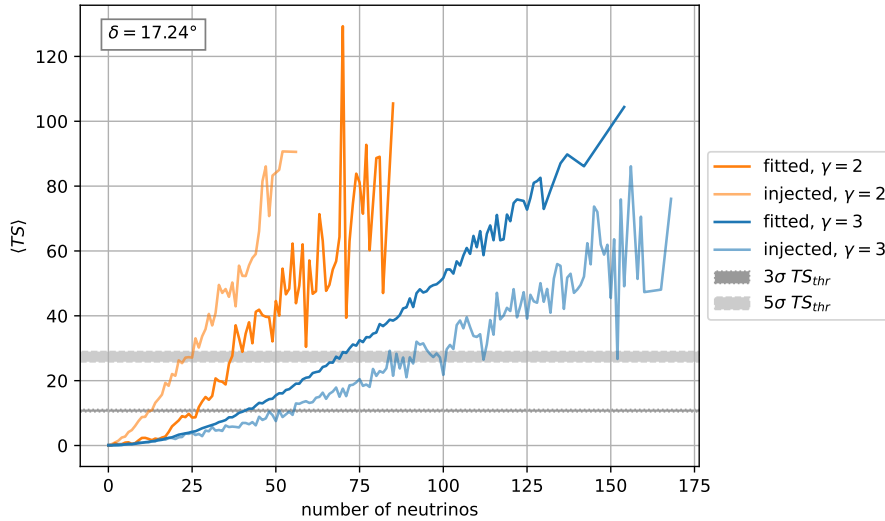


**Figure 4.1:** Evolution of the 50 % quantile of the  $TS$ -distribution as a function of the number of injected and fitted neutrinos for both spectral indices at  $\delta = 17.24^\circ$ . The threshold regions  $TS_{thr}$  are shown for the  $3\sigma$  and  $5\sigma$  discovery potential drawn from the background sample truncated at different  $TS$  values.

lished by the IceCube collaboration is scrambled in right ascension for each trial and used as a randomized pure background sample. The simulated events were added to the dataset. That approach is feasible because the data is highly dominated by background events (see section 2.4). Scrambling in right ascension is sufficient to create a random background sample because the data is uniform in right ascension but not in declination as described in section 2.4. For the analysis, the data is split into two hemispheres at the horizon  $\delta = -5^\circ$  and only the hemisphere containing the position of the simulated source will be analyzed. That split-sky approach is faster than always analyzing the complete sky. The amount of simulated events is negligible compared to the size of the original IceCube dataset, so the performance study should also be valid for the pure IceCube dataset.

This work will study the sensitivity and the discovery potential of IceCubePy v0.28.1 as a function of declination. It also covers the fit bias of the reconstructed parameters  $n_S$  and  $\gamma$ .

The effects of the fit bias of the number of signal neutrinos and the behavior of the discovery potential for a hard ( $\gamma = 2.0$ ) and a soft spectral index ( $\gamma = 3.0$ ) are shown in fig. 4.1 at  $\delta = 17.24^\circ$ . It shows the evolution of the median  $TS$  value for an increasing number of injected and fitted neutrinos. The orange curves show the evolution for  $\gamma = 2.0$  and the blue curves for  $\gamma = 3.0$ . The lighter curves of each color show the evolution depending on the injected (true) number of neutrinos and the darker curves depending on the fitted

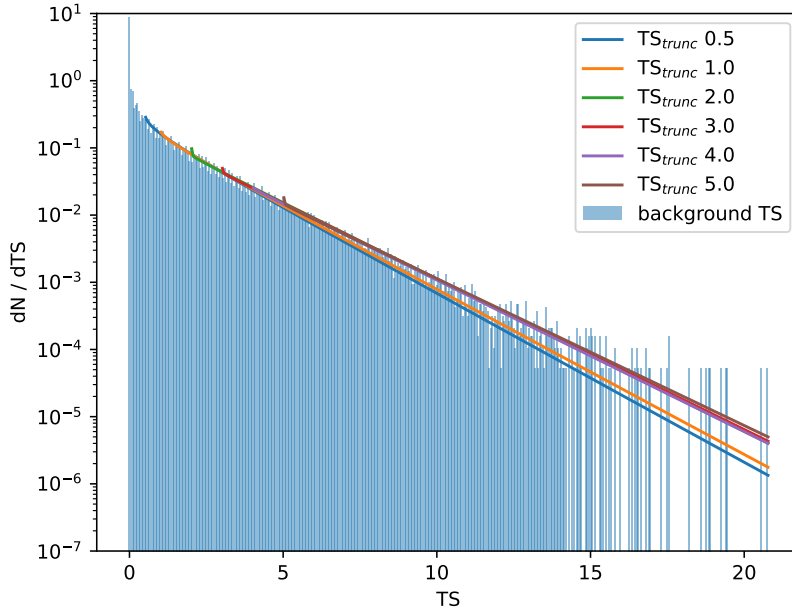


**Figure 4.2:**  $TS$  distribution of  $\sim 10^5$  background trials centered around  $\delta = 5.4^\circ$ . The data is truncated at 6 different  $TS$  values to fit a gamma distribution to the remaining data. This plot was provided by a collaborator.

number of neutrinos. The ranges of the threshold  $TS$  values for the  $3\sigma$  and the  $5\sigma$  discovery potential are shown in gray.

The difference between the injected number of neutrinos and the fitted number of neutrinos shows the effect of its fit bias. For high numbers of neutrinos, there are less simulations which leads to a loss in statistics and therefore enables higher fluctuations. We can see for  $\gamma = 2.0$ , the number of neutrinos is overestimated by the fit but it is underestimated for  $\gamma = 3.0$ . We also can see that the discovery potential is reached by a lower number of neutrinos for a hard spectral index compared to a softer spectral index. The performances of IceCubePy are characterized in the following sections in detail.

## 4.1 Sensitivity and Discovery Potential

To estimate the sensitivity and discovery potential of IceCubePy for searching astrophysical point sources, we used a large sample of background trials ( $\mathcal{O}(10^5)$  trials) at each studied declination (see fig. 4.2) that were analyzed to estimate the median  $TS$  value  $\langle TS_{bkg} \rangle$ , which should by design be zero for an infinite number of trials. Since we used a finite number of trials, small deviations from that expectation are possible. This large

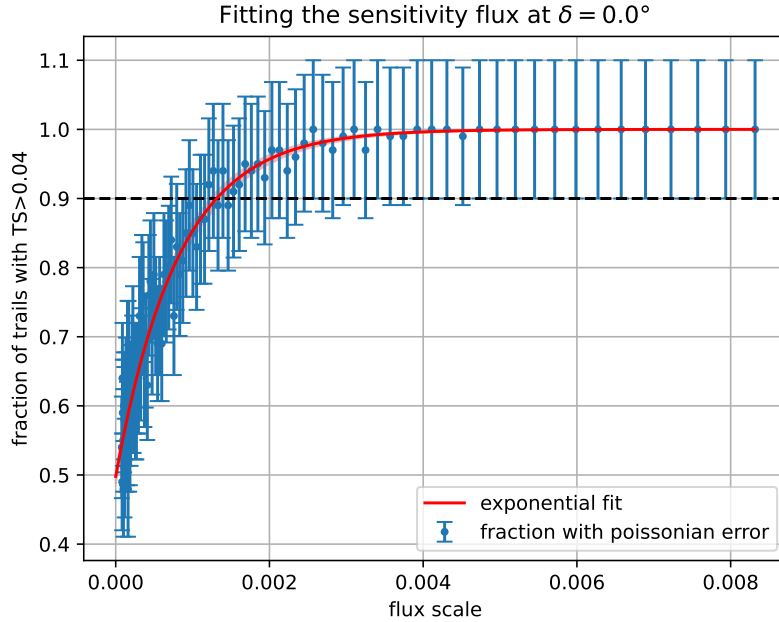


**Figure 4.3:** The fraction of trials with a  $TS$  value higher than the median  $TS$  value of background simulations at a declination  $\delta = 0^\circ$  for different simulated fluxes with an injected spectral index  $\gamma = 2.0$ . The flux is given in code units (fraction of diffuse astrophysical flux). An exponential function is fitted to the data. The sensitivity flux is the flux, where the fitted exponential function has a value of 0.9, depicted with the black dashed line.

sample of background trials was produced by a collaborator. To estimate the sensitivity flux, at each simulated declination for each injected flux value the fraction of trials with a  $TS$  value higher than the  $TS$  threshold value  $TS_{thr} = \langle TS_{bkg} \rangle$  is plotted as a function of the injected flux. Then an exponential function was fitted to the fraction as a function of the injected flux:

$$f(x) = 1 - e^{-ax+b} \quad (4.1)$$

This is shown in fig. 4.3 for the simulation with spectral index  $\gamma = 2$  at declination  $\delta = 0^\circ$ . The uncertainty of the number of trials with a  $TS$  value higher than the median of the background is assumed to be poissonian.

The estimation of the  $3\sigma$  ( $5\sigma$ ) discovery potential flux of IceCubePy is done similarly to the estimation of the sensitivity flux described above. Here, the threshold  $TS$  value  $TS_{thr}$  is the  $TS$  value corresponding to a one-tailed p-value equivalent to a  $3\sigma$  ( $5\sigma$ ) Gaussian significance drawn from a gamma distribution fit to the large background sample truncated at a  $TS$  value  $TS_{trunc}$  (see fig. 4.2). Truncating the distribution at a  $TS$  value higher than zero makes the fit more accurate in describing the tail of the distribution.



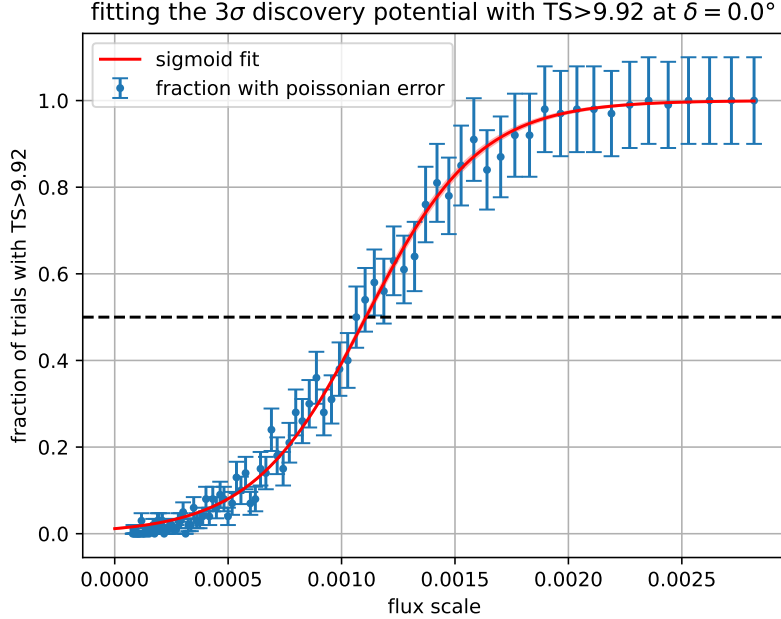


**Figure 4.4:** The fraction of trials with a  $TS$  value higher than the background  $TS$  value corresponding to a  $3\sigma$  p-value at a declination  $\delta = 0^\circ$  plotted as a function of injected flux. The flux is given in code units. A cumulative gamma function is fitted to the data without taking the poissonian error into account. The discovery potential flux is the flux, where the fitted cumulative gamma distribution has a value of 0.5, depicted with the black dashed line. In this plot, the injected spectral index is  $\gamma = 3.0$  and the threshold in  $TS$  was calculated using  $TS_{trunc} = 3.0$ .

Since this tail is the most relevant information for converting  $TS$  values to p-values, truncation is needed. We fitted the distribution truncated at 6 different  $TS$  values at all studied declinations to investigate the impact of different values on our quantities of interest. As depicted in fig. 4.2, the different truncations lead to a spread in the tail of the fitted gamma distribution. The fraction of trials with a  $TS$  value higher than the threshold value is plotted as a function of the injected flux in units of fractions of the astrophysical diffuse flux and a sigmoid function is fitted to the data:

$$f(x) = \left( 1 + \exp \left[ \frac{a - x}{b} \right] \right)^{-1} \quad (4.2)$$

In fig. 4.4 the fitting of the  $3\sigma$  discovery potential flux is shown at a declination  $\delta = 0^\circ$  for a point source with a spectral index  $\gamma = 3.0$  using the background  $TS$  distribution truncated at  $TS_{trunc} = 0.5$  to calculate  $TS_{thr}$ . Analogously to the sensitivity fit, the uncertainty of the number of trials with a  $TS$  value higher than the threshold  $TS$  value is assumed to be poissonian. Therefore, the error is zero for fluxes with no trials higher than the threshold, which would cause the fit to fail. To achieve a converging fit of the sigmoid function, the uncertainty of the fraction is not taken into account.

### 4.1.1 Sensitivity curve for $\gamma = 2.0$

The 90 % sensitivity, the  $3\sigma$  and the  $5\sigma$  discovery potential flux are calculated at all 21 simulated declinations as described above. The flux values are converted from the internal code units to physical flux units with a pivot energy of  $E_0 = 1$  TeV.

$$\frac{\partial\phi_{E_0}}{\partial E} = \text{flux\_scale} \cdot 4\pi \cdot \phi_{0,100\text{ TeV}} \cdot \left(\frac{E_0}{100\text{ TeV}}\right)^{-\gamma} \quad (4.3)$$

The factor  $4\pi$  guarantees that `flux_scale` is a fraction of the diffuse astrophysical flux detected by IceCube. For a pivot energy of 100 TeV according to the IceCube collaboration, the astrophysical diffuse flux is  $\phi_{0,100\text{ TeV}} = 1.44 \times 10^{-18} \text{ GeV}^{-1} \text{ cm}^{-2} \text{ s}^{-1} \text{ sr}^{-1}$  [38]. The converted sensitivity and discovery potential fluxes are plotted in fig. 4.5 as a function of  $\sin \delta$ .

The `IceCubePy` sensitivity for a spectral index  $\gamma = 2.0$  follows the declination dependency of the sensitivity published by the IceCube collaboration [2] but is in general a little bit worse. When comparing the sensitivity and also the discovery potential of `IceCubePy` to the ones published by the IceCube collaboration, it is important to notice that both analyses use different IRFs. `IceCubePy` uses the binned IRF published by the IceCube collaboration both for the simulation of the point source and for the likelihood analysis. In the analysis of the IceCube collaboration, the full IRF based on Monte Carlo simulations is used in both steps. Therefore, the observables of the injected neutrinos for a given flux and spectral index can be different between the `IceCubePy` analysis and the IceCube collaboration's analysis, so we are comparing sensitivities and discovery potentials estimated against signals that are potentially different. Therefore, a deviation in the sensitivity does not necessarily mean a deviation in the quality of the analysis.

In addition to the sensitivity published of by the IceCube collaboration, we compare the sensitivity of `IceCubePy` with the sensitivity of the analysis of the 10-year public dataset using `skyLLH`<sup>2</sup>, an open-source Python3-based package [40]. These sensitivity fluxes are calculated by a collaborator. We also compare our analysis to the sensitivity values presented by Bellenghi et al. [39], where they also used `skyLLH`. The sensitivity flux of `skyLLH` follows a similar trend in the declination dependence as the results from Bellenghi et al. [39]. In general, the `IceCubePy` sensitivity also follows this trend. The declinations near the poles show a somewhat larger deviation. At declination  $\delta = -5.67^\circ$ , the `IceCubePy` sensitivity deviates from all three reference values. The `IceCubePy` sensitivity flux is 48.77 % higher than the sensitivity flux presented by Bellenghi et al. [39], 68.50 % higher than the sensitivity flux of `skyLLH` calculated by a collaborator and 112.08 % higher than the sensitivity of the analysis of the IceCube collaboration [2]. That can be explained

<sup>2</sup><https://github.com/icecube/skylh>

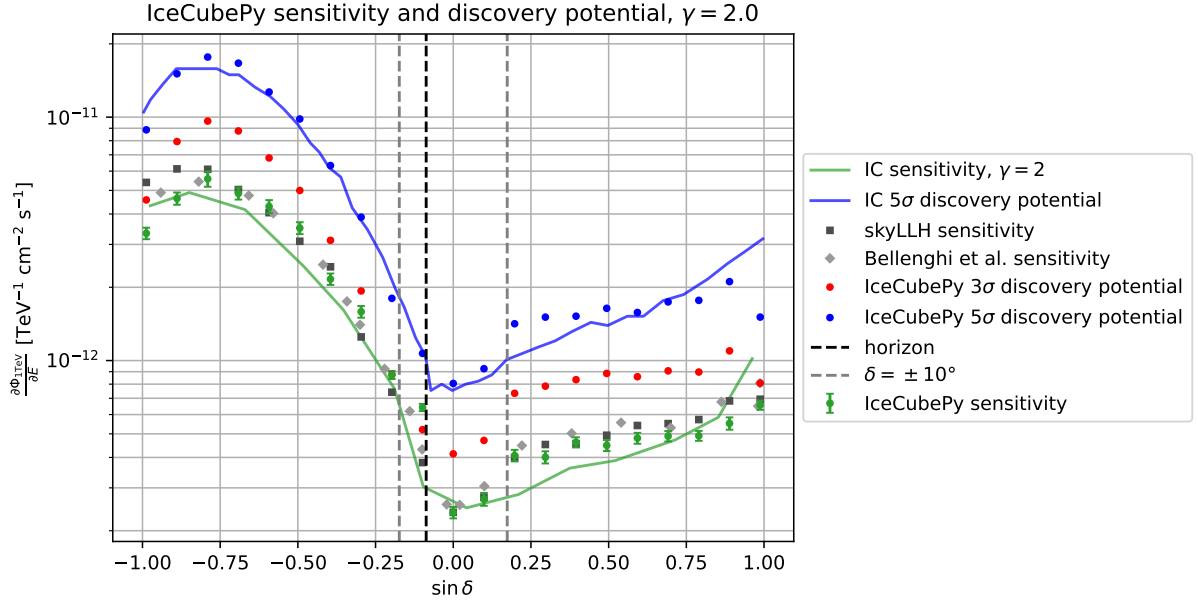


**Figure 4.5:** Sensitivity,  $3\sigma$  and  $5\sigma$  discovery potential flux of IceCubePy for an injected point source with spectral index  $\gamma = 2.0$  plotted as a function of  $\sin \delta$ . The shown discovery potential fluxes are calculated using  $TS_{trunc} = 3.0$ . As a reference, the sensitivity and the  $5\sigma$  discovery potential published by the IceCube collaboration (IC) [2], the sensitivity of an analysis performed by Bellenghi et al. [39] and the sensitivity of skyLLH (calculated by a collaborator) are plotted.

by the design of the IceCubePy split-sky analysis. Due to the different composition of the background in the northern and southern hemispheres, we split the dataset at the horizon ( $\delta = -5^\circ$ ) and analyze only the hemisphere at which the signal was injected. The injected signal is spread out according to the signal PDF (see section 3.2). When injecting a signal very close to the horizon, the signal gets diluted since the background is cut at the horizon. Therefore, a much higher flux is needed to reach the sensitivity of this analysis at  $\delta = -5.67^\circ$ .

Another deviation of the sensitivity results by IceCubePy, skyLLH and Bellenghi et al from the IceCube collaboration results can be observed around  $\delta = 10^\circ$ . The three analyses jump to worse sensitivities for  $\delta > 10^\circ$ . For increasing declination, the sensitivity flux increases slower than the reference by the IceCube collaboration. For  $\delta > 52.2^\circ$  the IceCubePy analysis has a lower sensitivity flux than the results from the IceCube collaboration. A reason for that can be, that the IceCube collaboration published their IRF only in three bins of declination: the southern hemisphere ( $\delta < 10^\circ$ ), the horizon region ( $\delta \in [-10^\circ, 10^\circ]$ ) and the northern hemisphere ( $\delta > 10^\circ$ ) [19]. For their analysis, the IceCube collaboration used full Monte-Carlo simulations which have not been publicly released at the time of writing. We can not see the same effect at  $\delta = -10^\circ$  since the sensitivity values from all references roughly agree with the IceCubePy flux at  $\delta = -11.39^\circ$ .

For lower declinations, we see a shift towards higher sensitivity fluxes in the IceCubePy data with respect to the sensitivity published by the IceCube collaboration. That shift decreases in decreasing declination, at the three most southern declinations, the IceCubePy sensitivity flux is compatible with the data published by the IceCube collaboration or lower. The sensitivity flux of skyLLH and the one published by Bellenghi et al. [39] also show an offset toward higher sensitivity fluxes but not as much decrease towards the south pole as IceCubePy.

There are no publications of the  $3\sigma$  discovery potential flux to compare with the performance of the IceCubePy analysis. The IceCube collaboration published the  $5\sigma$  discovery potential curve together with the sensitivity flux [2]. It shows, that the  $5\sigma$  discovery potential flux follows the declination dependence of the sensitivity flux while corresponding to higher flux values (as expected). Therefore, I will compare the  $3\sigma$  discovery potential to the sensitivity flux of IceCubePy. The  $3\sigma$  discovery potential flux follows in general the declination dependence of the IceCubePy sensitivity flux with an expected offset towards higher fluxes. There are two deviations from this general trend visible in fig. 4.5: At  $\delta = -5.67^\circ$  the discovery potential flux is lower than the sensitivity flux. Since at the current stage, the analysis is not reliable at this declination as pointed out above, I will not go into detail about that. At  $\delta = -11.39^\circ$ , the  $3\sigma$  discovery potential flux is roughly equal to the sensitivity flux. When comparing it to the sensitivity published by the IceCube collaboration, it looks like a dip in the IceCubePy  $3\sigma$  discovery potential flux at that declination. At  $\delta = 81^\circ$ , the  $3\sigma$  discovery potential flux decreases with respect to the sensitivity. That could be due to difficulties in the analysis near the poles.

In fig. 4.5 the  $3\sigma$  discovery potential flux is shown only for  $TS_{trunc} = 3.0$  but was calculated for the 6 different truncation values. The mean difference between the minimum and the maximum  $3\sigma$  discovery potential flux due to the choice of the truncation value per declination is 3.60% with a maximum difference of 10.04% at  $\delta = -81^\circ$ .

The IceCubePy  $5\sigma$  discovery potential flux is shown in blue in fig. 4.5. It is calculated analogously to the  $3\sigma$  discovery potential flux for six different truncation values of the background  $TS$  distribution. The choice of the truncation value has a larger impact on the  $5\sigma$  discovery potential flux than on the  $3\sigma$  discovery potential flux, namely a mean difference between the minimum and the maximum  $5\sigma$  discovery flux per declination of 6.54% and a maximum difference of 16.41%. The reason for that is that the tail of the fit to the background distribution is more sensitive to change in the truncation value because there is less data. This can be seen in fig. 4.2. For  $\delta < 10^\circ$ , the IceCubePy  $5\sigma$  discovery potential flux follows the  $5\sigma$  discovery potential published by the IceCube collaboration. At  $\delta = -81^\circ$ , it is lower than the IceCube reference, analog to the IceCubePy sensitivity.

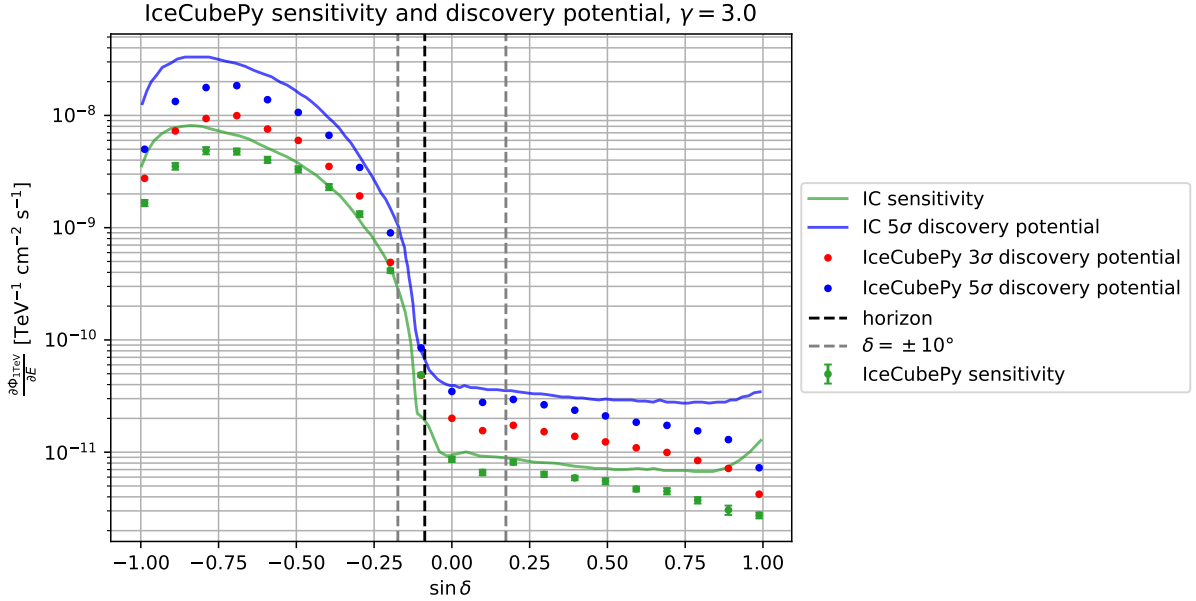


**Figure 4.6:** Sensitivity,  $3\sigma$  and  $5\sigma$  discovery potential flux of IceCubePy for an injected point source with spectral index  $\gamma = 3.0$  plotted as a function of  $\sin \delta$ . The shown discovery potential fluxes are calculated using  $TS_{trunc} = 3.0$ . As a reference, the sensitivity and  $5\sigma$  discovery potential flux published by the IceCube collaboration (IC) [2] are plotted.

At  $\delta = 10^\circ$ , a jump to higher flux values occurs analogously to the sensitivity and  $3\sigma$  discovery potential fluxes. As already described for the other two properties, a slower increase of the IceCubePy  $5\sigma$  discovery potential flux with increasing declination than the discovery potential flux published by the IceCube collaboration is observed. For  $\delta \geq 52.2^\circ$ , the IceCubePy analysis shows a lower  $5\sigma$  discovery potential flux than the results from the IceCube collaboration.

#### 4.1.2 Sensitivity curve for $\gamma = 3.0$

Analogously to the simulations with spectral index  $\gamma = 2.0$ , the sensitivity flux,  $3\sigma$  and the  $5\sigma$  discovery potential flux are fitted to the simulations of point sources with spectral index  $\gamma = 3.0$ . The fitted flux values are plotted as a function of  $\sin \delta$  in fig. 4.6 together with the sensitivity flux and the  $5\sigma$  discovery potential flux of the IceCube collaboration's analysis with  $\gamma = 3.0$  [2]. The data show that the IceCubePy sensitivity flux follows roughly the trend of the IceCube sensitivity flux but is at the most declinations lower. In the northern hemisphere, the IceCubePy sensitivity flux decreases more steeply with increasing declination than the sensitivity published by IceCube. In the southern hemisphere, the IceCubePy sensitivity flux is also lower than the IceCube reference when approaching the south pole. At  $\delta = -5.67^\circ$ , the sensitivity flux is 140.10% higher than the value published by IceCube. The reason is discussed in section 4.1.1. Analog to the

sensitivity curve for spectral index  $\gamma = 2.0$ , a small jump to higher values is visible around  $\delta = 10^\circ$  due to the binning of the published IRF. The IceCube sensitivity curve rises when approaching the north pole. That trend is not present in the IceCubePy result, which continues the decreasing trend over the complete northern hemisphere.

As already stated in section 4.1.1, there are no publications of the  $3\sigma$  discovery potential flux for a comparison to the IceCubePy performance. For spectral index  $\gamma = 3.0$ , it is also true that the published  $5\sigma$  discovery potential flux follows the declination dependence of the sensitivity flux while corresponding to higher flux values. The same can be stated for the IceCubePy results. Similar to  $\gamma = 2.0$ , at  $\delta = -5.67^\circ$  the discovery potential flux does not jump significantly to a higher value resulting in a similar flux value as the sensitivity flux at that declination. At  $\delta = -11.39^\circ$ , the sensitivity and  $3\sigma$  discovery potential flux are at a similar value with the sensitivity flux being lower than the  $3\sigma$  discovery potential flux. At  $\delta = 81^\circ$ , the  $3\sigma$  discovery potential flux decreases more than the sensitivity flux. The discovery potential was calculated for all six truncation values. The mean difference between the maximum and minimum  $3\sigma$  discovery potential flux due to the choice of the truncation value  $TS_{trunc}$  is 3.23% and the maximum difference is 10.57% at  $\delta = -81^\circ$ , so the influence of the choice of the truncation value is very similar to the sample with  $\gamma = 2.0$ .

Similarly to the behavior with spectral index  $\gamma = 2.0$ , the IceCubePy  $5\sigma$  discovery potential flux for spectral index  $\gamma = 3.0$  follows roughly the trend of the reference published by the IceCube collaboration. It follows the declination dependence of the IceCubePy  $3\sigma$  discovery potential flux while corresponding to higher values. The  $5\sigma$  discovery potential flux is comparable to the one published by the IceCube collaboration. It is more affected by the choice of the truncation value  $TS_{trunc}$  to calculate the threshold  $TS_{thr}$  than the  $3\sigma$  discovery potential flux. Here, the mean difference between the maximum and the minimum  $5\sigma$  discovery potential flux due to the choice of the truncation value is 5.89% and the maximum difference is 14.53% at  $\delta = -81^\circ$ . The influence of the choice of the truncation value on the discovery potential flux is similar to the sample with  $\gamma = 2.0$ .

## 4.2 Reconstruction of Spectral Parameters

When fitting parameters to data with a statistical method, it is important to know the systematic errors of this fit. In our case of the point source search in IceCube data with the unbinned likelihood analysis, the number of signal neutrinos  $n_S$  and the spectral index of the source  $\gamma$  are reconstructed. The fit bias shows the relation between the reconstructed parameter and the true injected parameter. The fit bias test is performed for both data samples (point sources with spectral indices  $\gamma \in \{2.0, 3.0\}$ ) for both reconstructed pa-

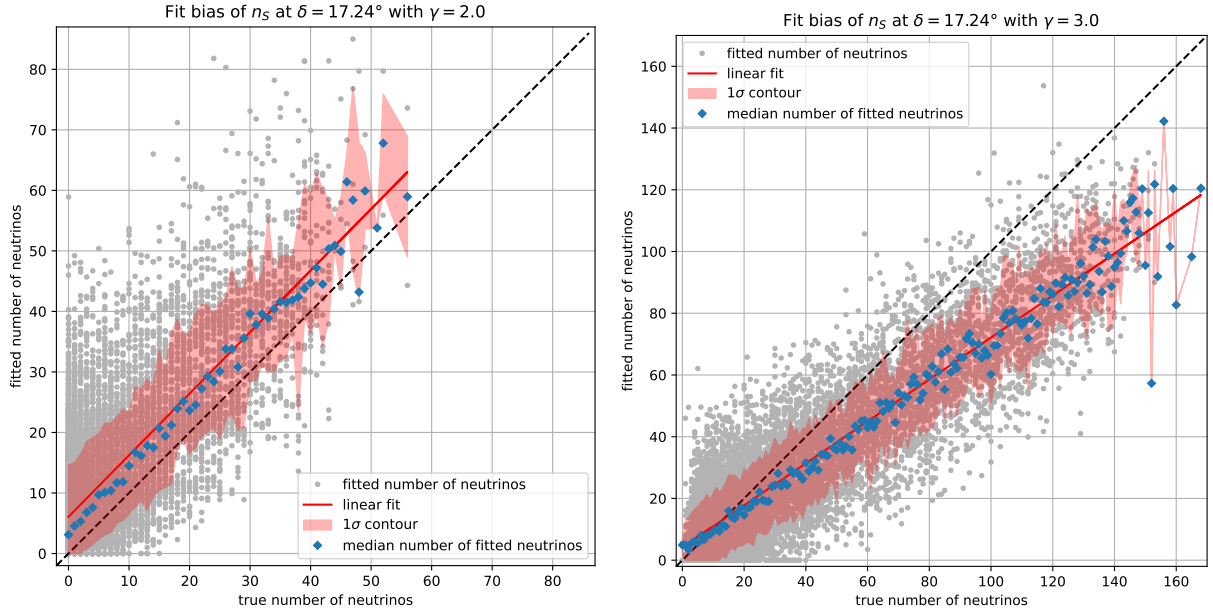


**Figure 4.7:** The number of signal neutrinos fitted by IceCubePy is plotted as a function of the true number of signal neutrinos. This plot shows the relation at the declination  $\delta = 17.24^\circ$  for a spectral index  $\gamma = 2.0$  (left) and  $\gamma = 3.0$  (right).

rameters  $n_S$  and  $\gamma$ .

### 4.2.1 Observed vs True Number of Events

The fit bias of the number of neutrinos  $n_S$  is performed at each simulated declination. To visualize this, the relation between the fitted number of neutrinos and the true number of neutrinos is plotted together with the contour containing 68% of the data and a fitted linear function is shown in fig. 4.7. The median fitted number of signal neutrinos follows roughly the linear fit but the data shows large scattering in the fitted number of signal neutrinos. There are not many simulations for high true numbers of neutrinos. Therefore, the median fitted number of neutrinos shows more scattering than for lower true numbers of neutrinos and the 68% contour is not representative. In this region, the linear fit might represent the actual behavior better than the median and the 68% contour. The plots showing the fit bias of the number of neutrinos for all declinations and both data samples are shown in the appendix (figs. A.1 and A.2).

In his PhD thesis work, T. Glauch [3] covers the fit bias of two different maximum likelihood analyses for point sources in 7 years of IceCube data [36]. They compare the analysis method of the IceCube collaboration that follows the unbinned likelihood test approach with a likelihood analysis using deep neural networks. The fit biases of the number of

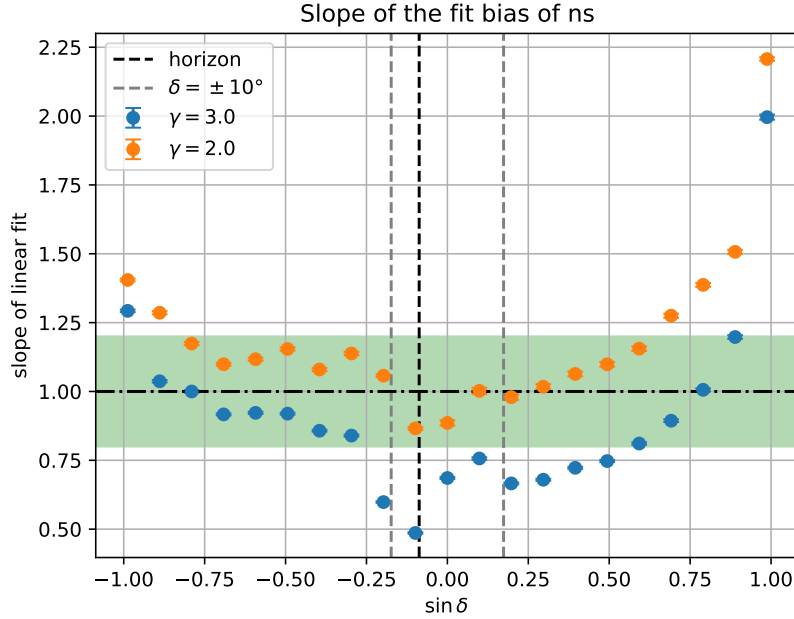


**Figure 4.8:** The slope of the linear function fitted to the relation between the fitted and the true number of neutrinos is plotted against the sine of the declination for a spectral index of 2.0 and 3.0. A slope  $> 1$  means that the number of neutrinos is overestimated by the analysis and a slope  $< 1$  shows an underestimation. A 20% band around slope=1 is shown in green.

signal events and the spectral index from these two analyses are shown in the PhD thesis of T. Glauch in figures 7.18 and D.7 with a true spectral index  $\gamma = 2.0$  and figures 7.19 and D.8 with a true spectral index  $\gamma = 3.2$ . Since the first analysis uses the same approach as IceCubePy, I compare IceCubePy to this analysis' fit bias shown by T. Glauch. Since they present the results for declinations that are not simulated in my data samples, we compare their results with the IceCubePy results at the nearest covered declination. Their sample of positions contains only declinations in the northern hemisphere and they show results for the spectral indices  $\gamma = 2.0$  and  $\gamma = 3.25$ , so I can only directly compare the two methods for  $\gamma = 2.0$ . For the softer index, I can only compare if both methods show the same differences between a soft and a hard index. Because of the large scattering in the fitted number of neutrinos, resulting in a large  $1\sigma$  uncertainty band, the IceCubePy results are in general compatible with the results shown by T. Glauch [3] when comparing close values of declination for both indices.

The slope of this linear fit can be used as a quantitative measure of the fit bias. The y-intercept of the fit cannot be used as a measure because the background varies with the declination and influences the y-intercept. The slope of the fit bias is shown in fig. 4.8 as a function of  $\sin \delta$  for both spectral indices. It shows that the number of neutrinos is the



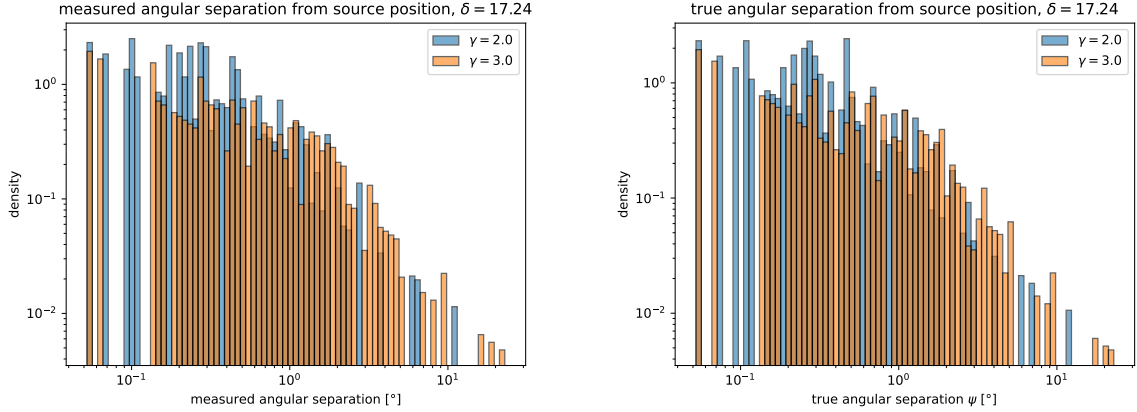


**Figure 4.9:** Angular separation between the simulated events and the true point source position. The left histogram shows the distribution of the angular separation of the simulated neutrinos whereas the right histogram shows the distribution of the angular separation  $\psi$  that is used to sample the positions of the simulated events. Both histograms show that the simulation with spectral index  $\gamma = 3.0$  has higher maximum separations compared to the simulation with  $\gamma = 2.0$ . The distributions of  $\psi$  for different energy bins are shown in [19].

most overestimated at the poles and the most underestimated at the horizon. Both spectral indices show the same trend, but the data sample with spectral index  $\gamma = 3.0$  shows an offset towards lower slopes. In fig. 4.8 one can see that *IceCubePy* can reliably recover the number of signal neutrinos (20% band around slope=1) for hard indices roughly in the range  $-0.8 \lesssim \sin \delta \lesssim 0.6$  when excluding the region around the horizon ( $\delta = -5^\circ$ ) as argued in section 4.1.1. For softer indices, it can reliably recover the number of signal neutrinos roughly in the two ranges  $-0.9 \lesssim \sin \delta \lesssim -0.3$  and  $0.6 \lesssim \sin \delta \lesssim 0.8$ . To make the claim about these roughly estimated ranges more reliable, further studies are needed. Regardless of the bias in fitting the spectral parameters  $n_S$  and  $\gamma$ , the sensitivity and discovery potential discussed above are still reliable as long the simulation of the signal is reliable.

A reason for the difference in the fit bias of the reconstructed number of signal neutrinos between the spectral indices could be differences in the spatial distribution of the simulated point source. Signal events are simulated by sampling the angular separation  $\psi$  between the source position and the event position from the IRF. Then, the right ascension and declination values are sampled from that. We measured the angular separation of the simulated events sampled from the  $\psi$  values. When looking at the distribution of the measured angular separation in fig. 4.9, one can see that for a spectral index  $\gamma = 3.0$  the most distant neutrinos have a larger angular separation than for a spectral index  $\gamma = 2.0$ . The same can be observed in the distribution of the  $\psi$  values. The distribution of the  $\psi$

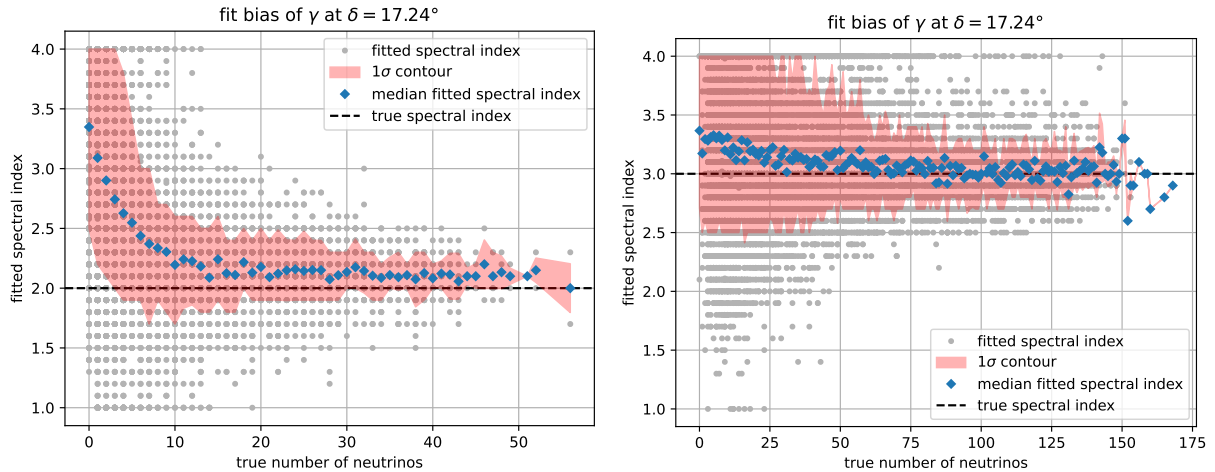


**Figure 4.10:** The spectral index reconstructed by IceCubePy is plotted as a function of the true number of signal neutrinos. This plot shows the behavior of the reconstructed spectral index for a true spectral index  $\gamma = 2.0$  (left) and  $\gamma = 3.0$  (right) at  $\delta = 17.24^\circ$ .

value in different energy bins of the public data release is shown in fig. 3 of [19]. It is possible that deviations between the distribution of  $\psi$  and the measured angular separation occur which are larger than deviations caused by effects of numerical approximation since the injection code might not be able to reliably sample the event's coordinates for large values of  $\psi$  (in the order of  $10^\circ$ ). These badly reconstructed events will not contribute to the likelihood as they are suppressed by the spatial term in the PDF. Since the likelihood analysis uses the same point spread function to reconstruct the point source for both spectral indices, it classifies more neutrinos as signal neutrinos in the sample with index  $\gamma = 2.0$  compared to the sample with index  $\gamma = 3.0$ . That can explain the offset in fig. 4.8 between the two indices [16] but a more detailed study is needed to confirm that.

## 4.2.2 Observed vs True Spectral Index

Similar to the fit bias of the number of signal neutrinos, the fit bias of the spectral index is performed at each simulated declination for both true spectral indices  $\gamma = 2.0$  and  $\gamma = 3.0$ . These relations are shown in fig. 4.10, where the reconstructed spectral index is plotted as a function of the true number of signal neutrinos together with the median reconstructed index, a contour containing 68% of the simulations and the true spectral index. No function is fitted to the data since there is no uniform behavior across both data samples. The plots showing the fit bias of the spectral index for all declinations and both data samples are shown in the appendix (figs. A.3 and A.4). As stated in section 4.2.1, there are less simulations with a high true number of neutrinos which causes a higher scattering in the median compared to lower true numbers of neutrinos.

For all declinations, the fitted index converges to a value close to the true spectral index when the number of neutrinos is high. In the data sample with a true spectral index  $\gamma = 2.0$ , the median fitted index for low numbers of neutrinos is significantly higher than its true value. This deviation is in general larger in the northern hemisphere (fitted index  $\gamma > 3.0$  for zero true signal neutrinos) compared to the southern hemisphere (fitted index  $2.5 < \gamma \leq 3.0$  for zero true signal neutrinos). This is the expectation since for low numbers of signal neutrinos, the spectral index should get closer to the index of the atmospheric background. Due to the harsh energy cut applied to the data in the southern hemisphere, the background index tends to be harder in the southern hemisphere in this dataset. In the data sample with a true spectral index  $\gamma = 3.0$ , there are two different trends visible: In the northern hemisphere, the median fitted index is larger than the true index for low true numbers of neutrinos whereas in the southern hemisphere, the median fitted spectral index is lower than the true index for low true numbers of neutrinos. The only outlier in each of the data samples from the described trend is  $\delta = -81^\circ$  which shows the trend of the northern hemisphere.

When comparing the `IceCubePy` results with the results presented by T. Glauch (shown in figures 7.18 and D.7 with a true spectral index  $\gamma = 2.0$  and figures 7.19 and D.8 with a true spectral index  $\gamma = 3.2$ , [3]), we can see that both analyses show the same dependence on the true number of neutrinos and agree within their uncertainty bands.

In fig. 4.10, one can see that the fitted spectral index mostly has discrete values. That is caused by the choice of a fast interpolation method for the energy component of the PDF in the likelihood analysis. An alternative interpolation method producing a continuous distribution of fitted  $\gamma$  values has been implemented in `IceCubePy` during the development of this thesis.

## Chapter 5

# Conclusion and Outlook

This thesis presents the performance of the python based analysis software `IceCubePy` using an unbinned likelihood ratio test in terms of its sensitivity and discovery potential flux for the search of point sources and the bias of the fitted number of neutrinos and the fitted spectral index of a point source in the 10-year public dataset. In the analysis, the dataset was split into two hemispheres at the horizon  $\delta = -5^\circ$  and only the hemisphere containing the position of the simulated point source was analyzed (split-sky mode of `IceCubePy`). This was done for two samples of point source simulations with the spectral index  $\gamma = 2.0$  and  $\gamma = 3.0$  respectively. To calculate the sensitivity flux, the  $3\sigma$  and the  $5\sigma$  discovery potential flux, for each declination a threshold  $TS$  value  $TS_{thr}$  is drawn from the  $TS$  distribution of a large background sample. For each injected flux the fraction of trials with  $TS > TS_{thr}$  was calculated and an exponential function was fitted to the fractions calculated with the threshold for the sensitivity and a sigmoid function was fitted to the fractions calculated with the thresholds for the discovery potential, both as a function of the injected flux. The sensitivity flux,  $3\sigma$  and  $5\sigma$  discovery potential flux of `IceCubePy` were compared to the respective published quantities of the analysis of the IceCube collaboration [2]. Since the IRF used in `IceCubePy` both for the point source simulation and for the definition of the likelihood is different from the IRF that is used in the analysis of the IceCube collaboration in both steps, a difference in the sensitivity or discovery potential between these analyses does not necessarily mean that one them is a better analysis than the other one.

The sensitivity of `IceCubePy` for the search of point sources generally follows the IceCube sensitivity but is on average a bit worse for  $\gamma = 2.0$  and comparable for  $\gamma = 3.0$ . Due to the differences between the 10-year public dataset and the full dataset used by the IceCube collaboration, there are jumps to higher fluxes near the edges of the bins of the published instrument response function of the detector. Besides that artifact explained by the data quality, we found a deviation from the literature sensitivities at  $\delta = -5.67^\circ$

which is caused by the design of the analysis. That can be improved in upcoming versions of `IceCubePy`.

The discovery potential flux of `IceCubePy` also follows the data published by the IceCube collaboration but is a bit worse in the northern hemisphere for  $\gamma = 2.0$  and comparable in both hemispheres for  $\gamma = 3.0$ . The jump toward higher fluxes at the edges of the IRF bins is visible only in the northern hemisphere. There is no deviation from the literature discovery potential flux at  $\delta = -5.67^\circ$ . To define the threshold  $TS$  values to estimate the discovery potential, the tail of the background  $TS$  distribution is crucial. That tail can be best described by employing a truncated gamma distribution fit to the data. We used 6 different truncation values. The  $3\sigma$  discovery potential flux fluctuates due to different truncations by on average 3.60% (3.23%) for a spectral index  $\gamma = 2.0$  ( $\gamma = 3.0$ ) whereas the  $5\sigma$  discovery potential flux fluctuates by on average 6.54% (5.89%).

In the analysis of the bias in the fitted number of neutrinos, the mean fitted number of neutrinos as a function of the true number can be described with a linear function. The slope of this linear fit can be used as a quantitative measure but not the y-intercept due to the influence of the background, which varies with declination. Since there is a large scattering in the events, it may be difficult to correct for this bias for individual point sources. In general, for  $\gamma = 3.0$  we underestimate the number of neutrinos while we overestimate it for  $\gamma = 2.0$ . Based on the slope of the linear fit, `IceCubePy` seems to fit the number of neutrinos reliably (20% around slope=1) for  $\gamma = 2.0$  roughly in the range  $-0.8 \lesssim \sin \delta \lesssim 0.6$  when excluding the region around the horizon ( $\delta = -5^\circ$ ) and for  $\gamma = 3.0$  in the ranges  $-0.9 \lesssim \sin \delta \lesssim -0.3$  and  $0.6 \lesssim \sin \delta \lesssim 0.8$ . To make a more confident claim about that, more detailed studying of the performance is needed. Especially the region near the horizon should be studied with a finer binning in declination. Regardless of this limitation by the fit bias, the estimated sensitivity and discovery potential are reliable at all declinations as long as the simulation is reliable. When comparing the performance of `IceCubePy` with the performance shown by T. Glauch [3], the results agree with each other but both studies show a large uncertainty band.

The fitted spectral index converges to a constant value close to the true spectral index with an increasing true number of neutrinos at all simulated positions and for both true spectral indices. In the comparison with the results presented by T. Glauch [3], the results of both analyses agree within their uncertainties. `IceCubePy` returns most of the time a fitted spectral index with a discrete value rather than a continuous one. This issue can be improved using a slower interpolator method for the energy term of the PDF in the likelihood analysis.

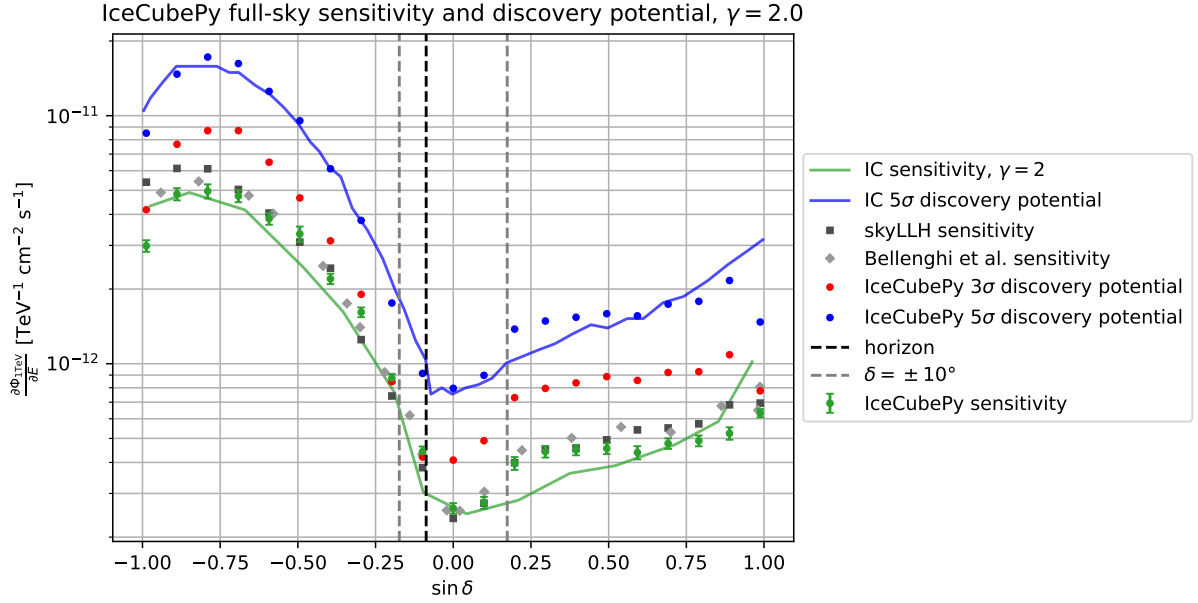


**Figure 5.1:** Sensitivity,  $3\sigma$  and  $5\sigma$  discovery potential flux of the full sky analysis of `IceCubePy` for an injected point source with spectral index  $\gamma = 2.0$  plotted as a function of  $\sin \delta$ . The shown discovery potential fluxes are calculated using  $TS_{trunc} = 3.0$ . As a reference, the sensitivity and the  $5\sigma$  discovery potential published by the IceCube collaboration (IC) [2], the sensitivity of an analysis performed by Bellenghi et al. [39] and the sensitivity of `skyLLH` (calculated by a collaborator) are shown.

`IceCubePy` can be used in a full-sky mode where the complete sky is considered for each analysis regardless of the source position. This mode was added to the tool to treat the region close to the horizon ( $\delta = -5^\circ$ ) appropriately. The sensitivity and both discovery potential fluxes of the full-sky analysis for a sample of simulations with spectral index  $\gamma = 2.0$  is shown in fig. 5.1 and fig. 5.2 shows the respective quantities for a sample of simulations with spectral index  $\gamma = 3.0$ . In both cases, the deviation from the literature sensitivities decreases. Also, the fit bias of the number of signal neutrinos close to the horizon improves using the full-sky mode for both spectral indices as depicted in fig. 5.3. The full-sky analysis is promising to treat the region close to the horizon more appropriately than the split-sky mode of `IceCubePy` but more detailed studies need to be done for this analysis mode.

Another performance that needs to be studied in more detail is the angular distribution of source neutrinos. That can explain the fit bias of the number of signal neutrinos presented in this work. `IceCubePy` can already be used for scientific studies and this work provides a well detailed characterization of its performances and limitations (mostly due to the

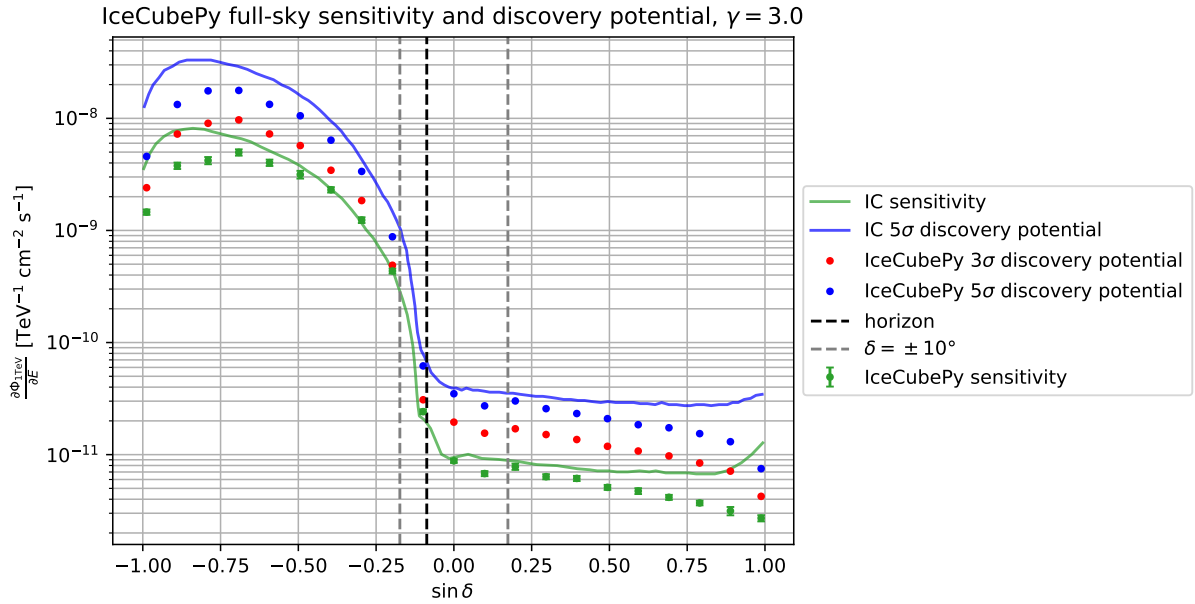


**Figure 5.2:** Sensitivity,  $3\sigma$  and  $5\sigma$  discovery potential flux of the full sky analysis of IceCubePy for an injected point source with spectral index  $\gamma = 3.0$  plotted as a function of  $\sin \delta$ . The shown discovery potential fluxes are calculated using  $TS_{trunc} = 3.0$ . As a reference, the sensitivity and the  $5\sigma$  discovery potential published by the IceCube collaboration (IC) [2] are shown.

properties of the public dataset). An example of a scientific study using IceCubePy could be to correlate the positions of neutrino hotspots with samples or catalogs of potential neutrino source candidates like blazars.

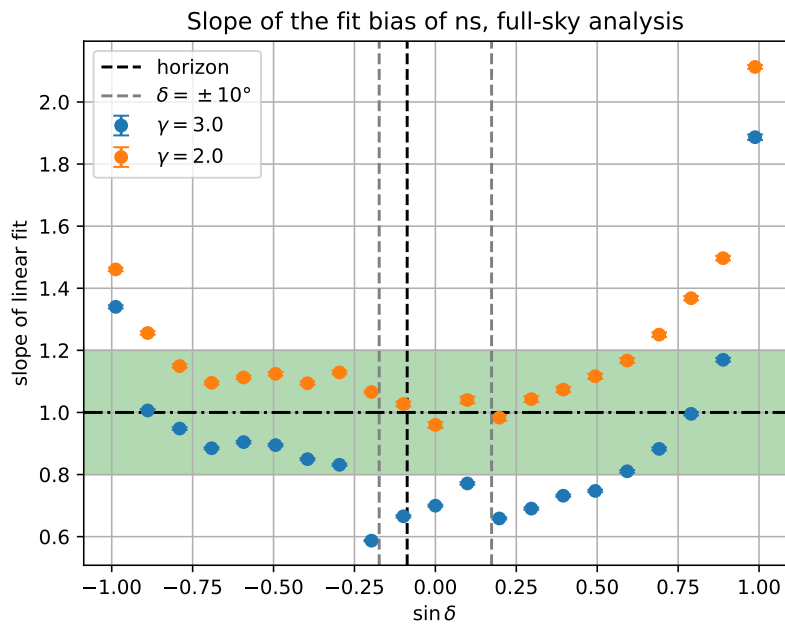


**Figure 5.3:** The slope of the linear function fitted to the relation between the fitted and the true number of neutrinos as a measure of the fit bias of the number of signal neutrinos using the full-sky analysis of IceCubePy is plotted against  $\sin \delta$  for a spectral index of 2.0 and 3.0. A slope  $> 1$  means that the number of neutrinos is overestimated by the analysis and a slope  $< 1$  shows an underestimation. A 20% acceptance area around slope=1 is shown in green.



## Acknowledgments

First, I want to thank Professor Sara Buson for the opportunity to work in the field of neutrino astronomy, all her answers to my questions and thereby even deepening my fascination for the universe. I enjoyed working in the great working environment of the *MessMapp* group. Thank you for your support during the time of my Bachelor thesis.

I also want to express my gratitude to my Massimiliano Lincetto, who always helped with his deep knowledge about *IceCubePy* and neutrino astronomy. He was always reachable despite working in a different city. Also, I want to thank him for proofreading my thesis.

I also want to thank Josè Maria Sanchez Zaballa for his work on the background trials which made parts of my thesis possible. I am also very thankful for all the time you offered to help with my challenges.

Lastly, I want to thank all the other members of the *MessMapp* group for sharing ideas and giving feedback in the weekly meetings and spontaneous breakout sessions. I also thank for the nice conversations on a daily basis.

This work was supported by the European Research Council, ERC Starting grant *MessMapp* under contract no. 949555.

Außerdem möchte ich meiner Familie danken, die mich immer unterstützt haben, sei es durch Telefonate oder auch zu Hause. Ihr habt mich in dieser Zeit immer wieder aufgebaut mit frischem Gebäck oder auch einfach Ablenkung, wenn ich mal wieder vor einem neuen Problem stand.

# Appendix A

## Fit Bias Plots

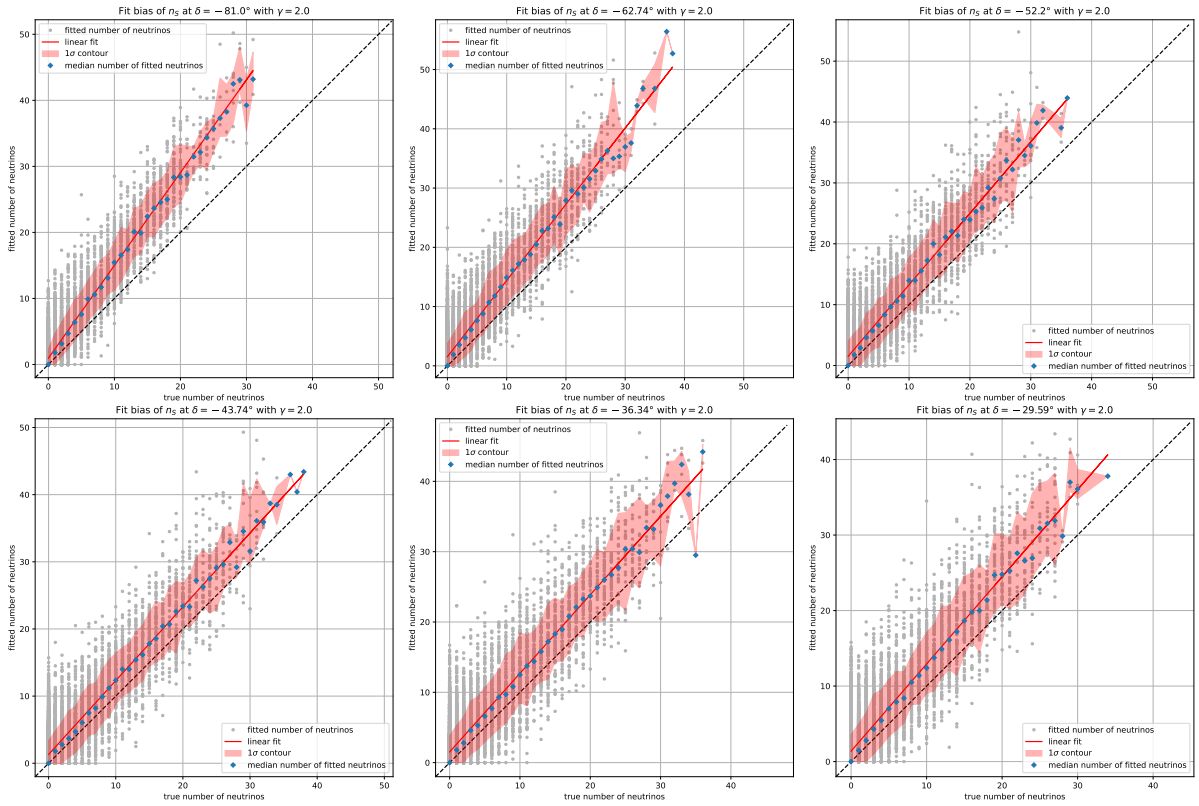


**Figure A.1:** Fit bias of the number of signal neutrinos for all simulated declinations with a true spectral index  $\gamma = 2.0$ .

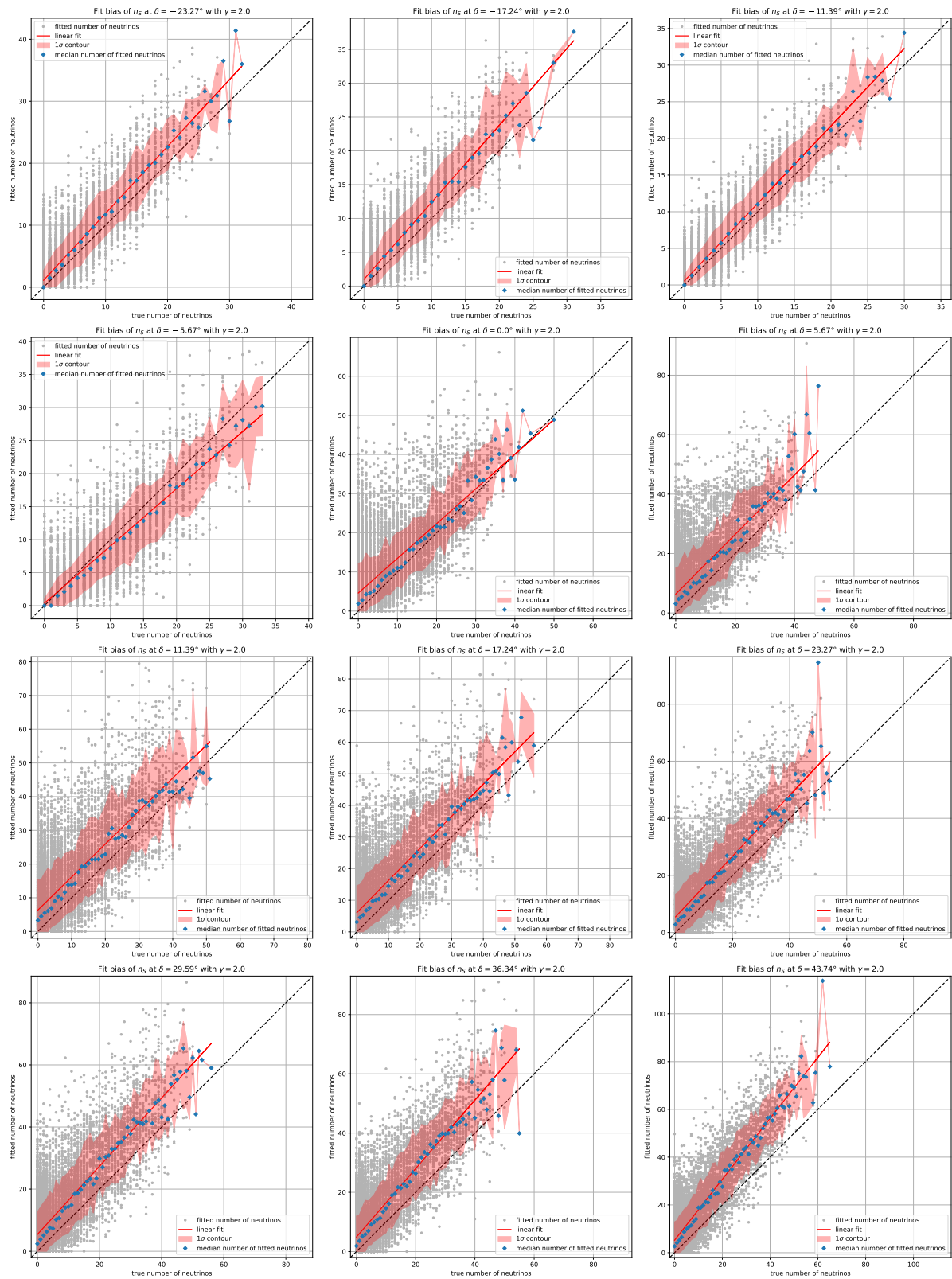


**Figure A.1:** Fit bias of the number of signal neutrinos for all simulated declinations with a true spectral index  $\gamma = 2.0$ .(cont.)

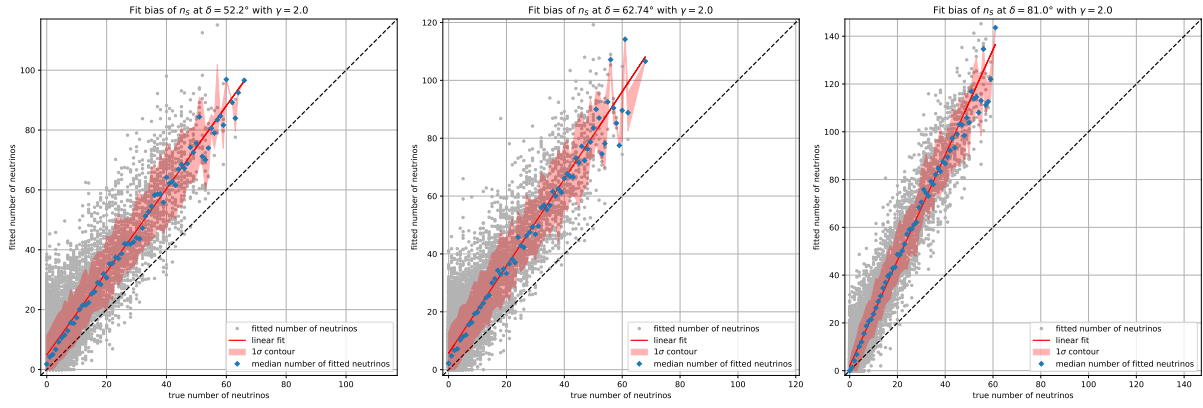


**Figure A.1:** Fit bias of the number of signal neutrinos for all simulated declinations with a true spectral index  $\gamma = 2.0$ .(cont.)

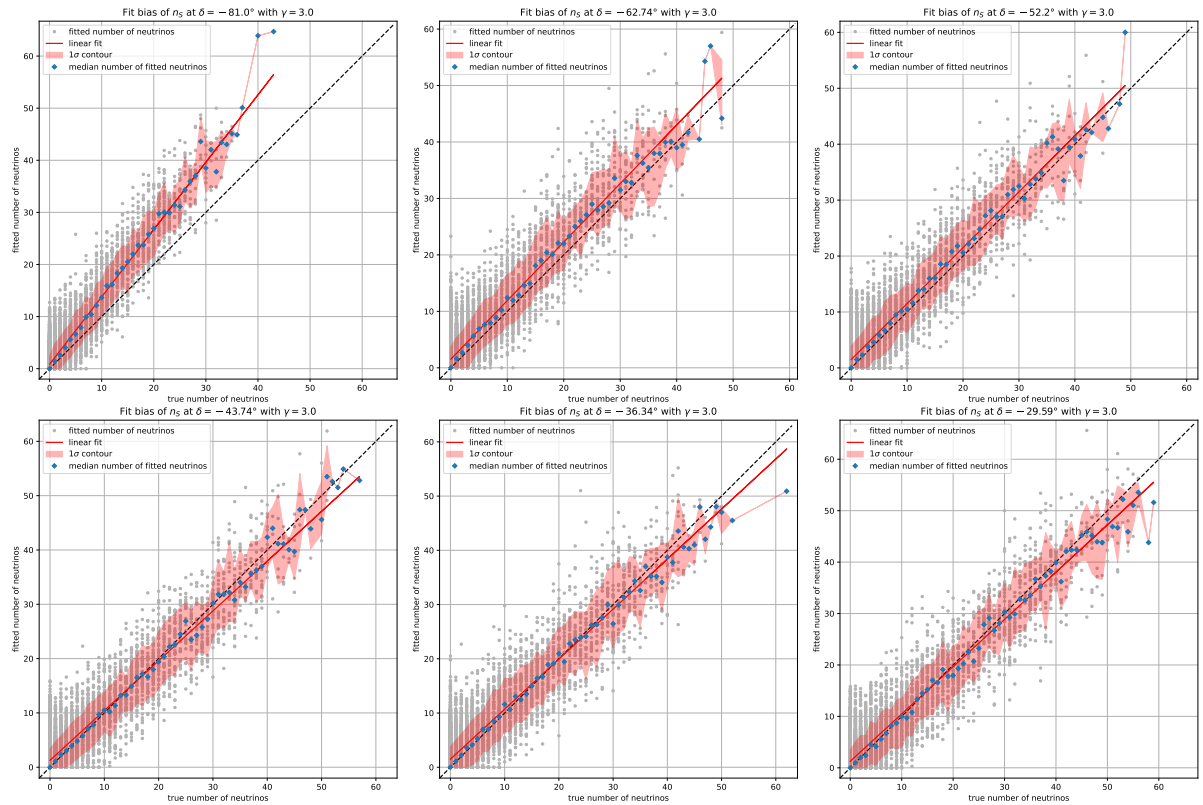


**Figure A.2:** Fit bias of the number of signal neutrinos for all simulated declinations with a true spectral index  $\gamma = 3.0$ .

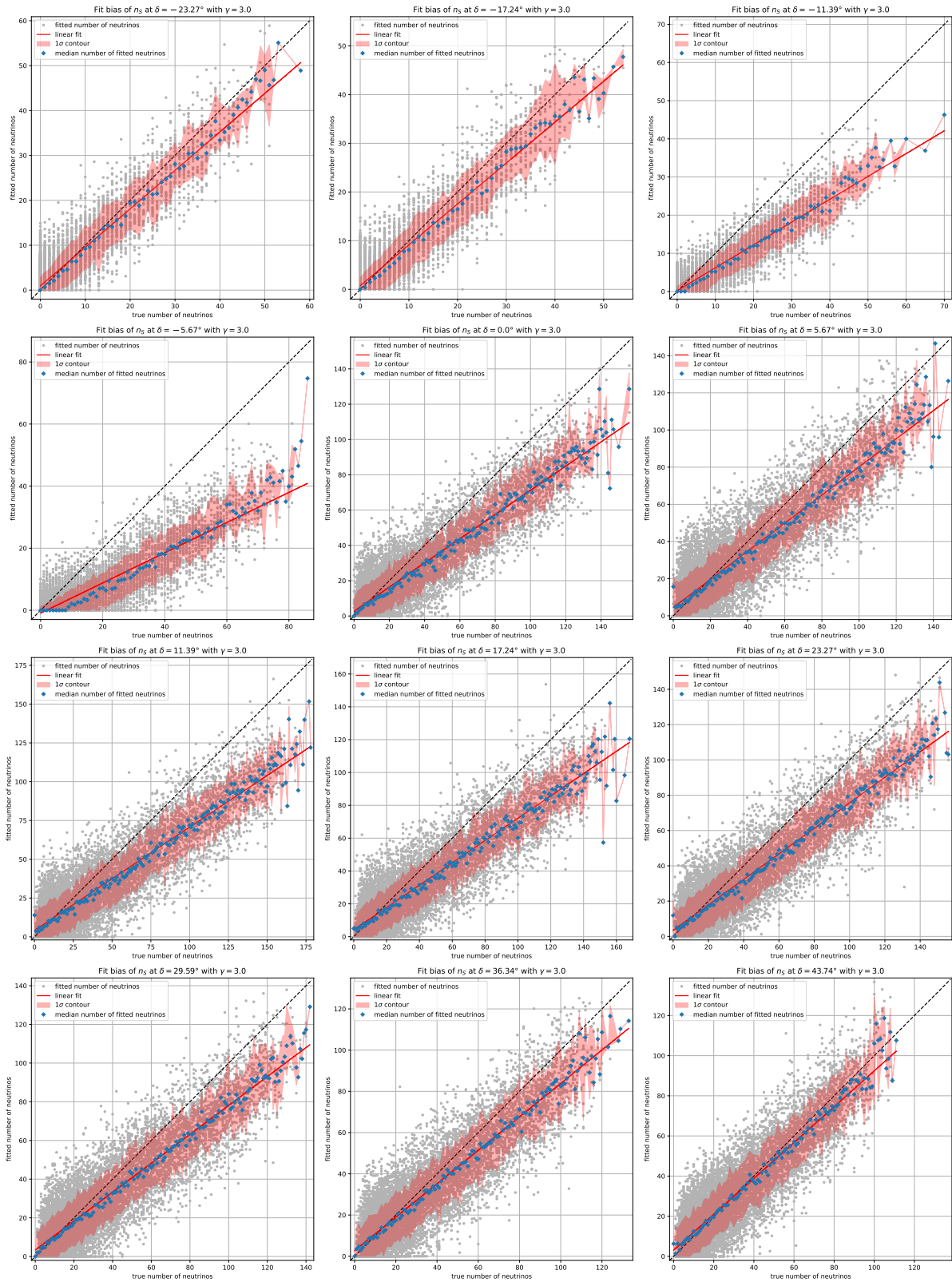


**Figure A.2:** Fit bias of the number of signal neutrinos for all simulated declinations with a true spectral index  $\gamma = 3.0$ . (cont.)

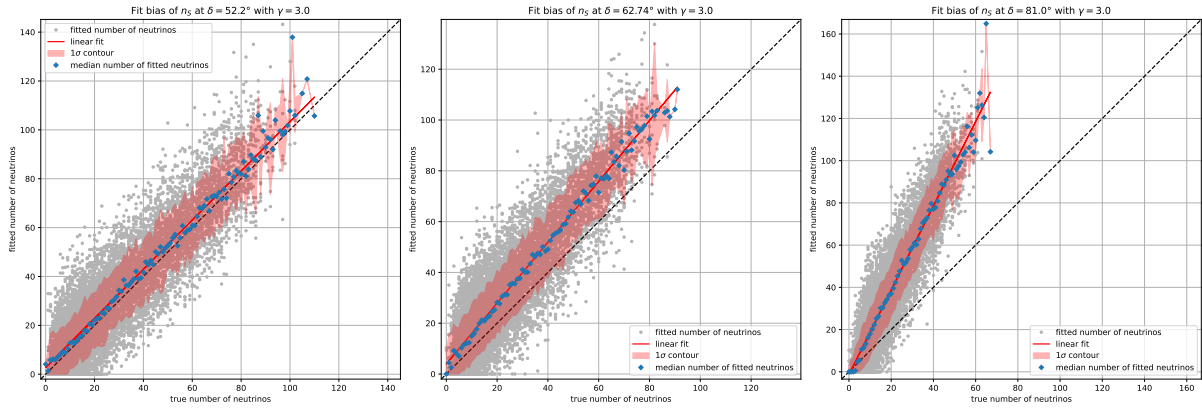


**Figure A.2:** Fit bias of the number of signal neutrinos for all simulated declinations with a true spectral index  $\gamma = 3.0$ .(cont.)

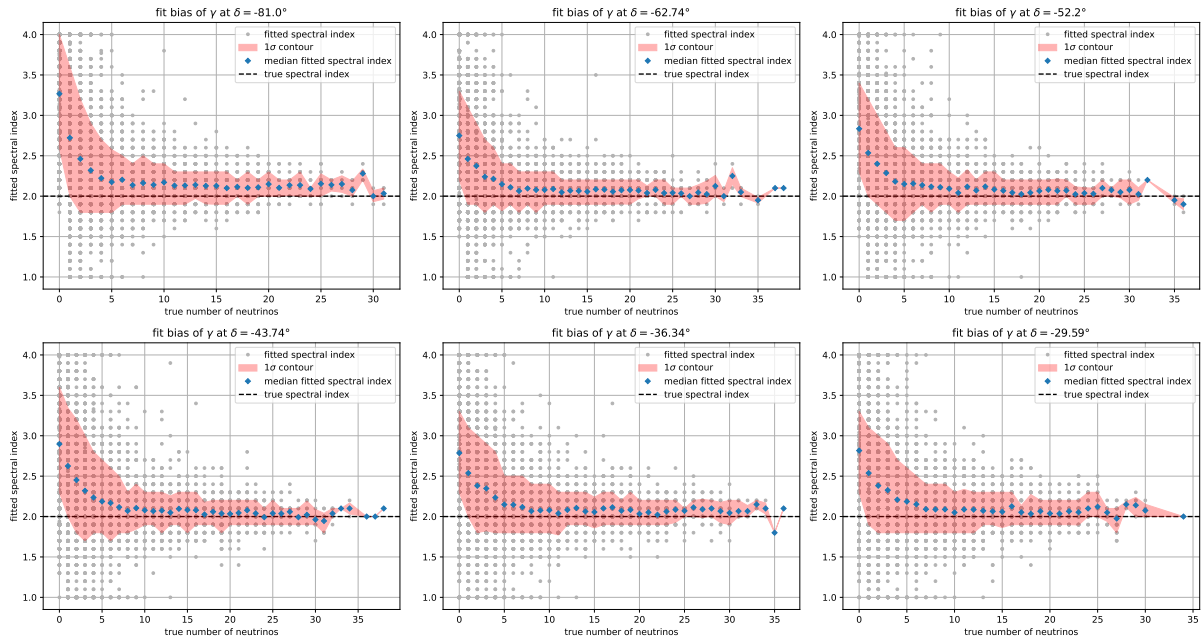


**Figure A.3:** Fit bias of the number of signal neutrinos for all simulated declinations with a true spectral index  $\gamma = 2.0$ .



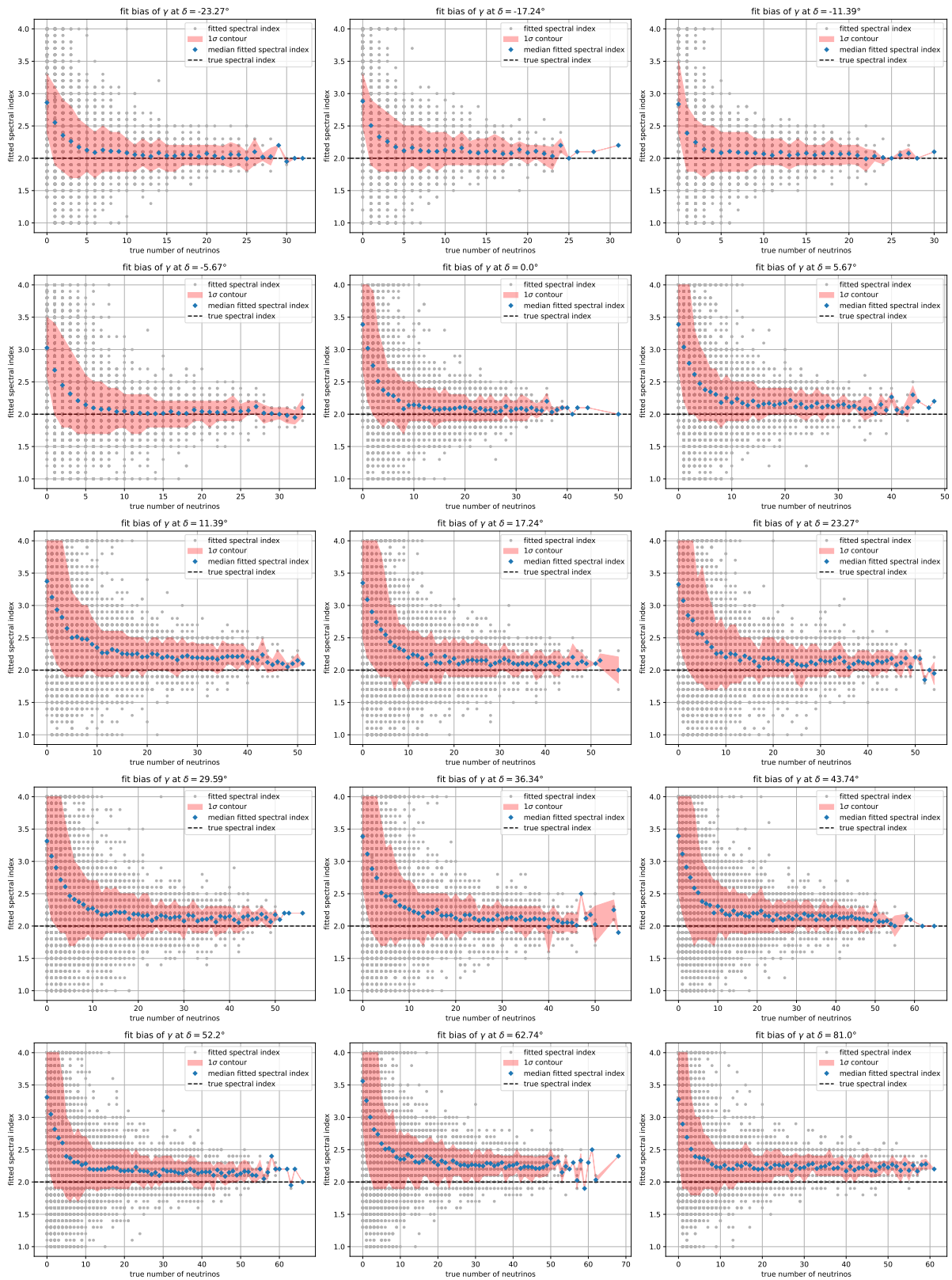


**Figure A.3:** Fit bias of the number of signal neutrinos for all simulated declinations with a true spectral index  $\gamma = 2.0$ . (cont.)

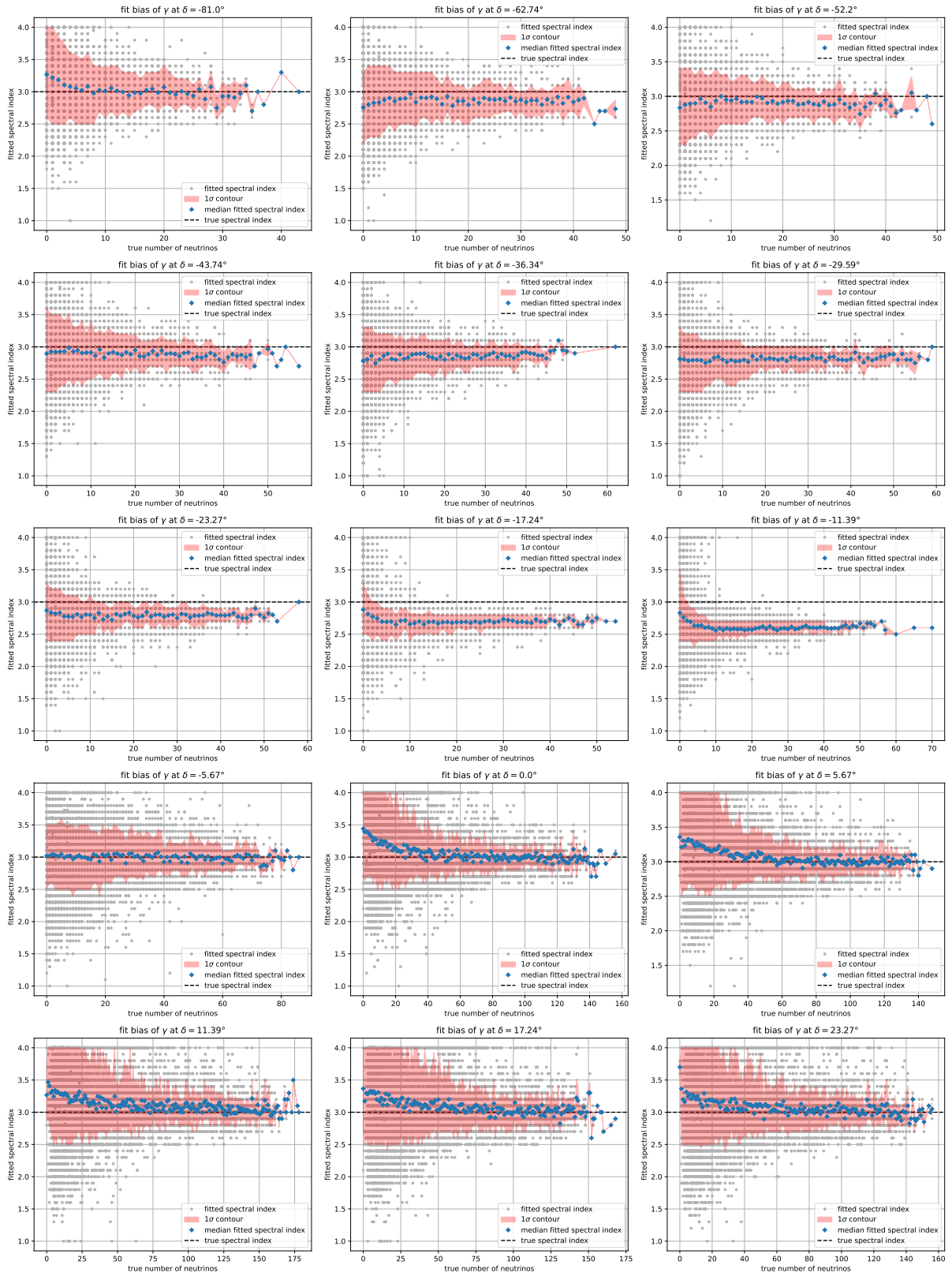


**Figure A.4:** Fit bias of the number of signal neutrinos for all simulated declinations with a true spectral index  $\gamma = 3.0$ .



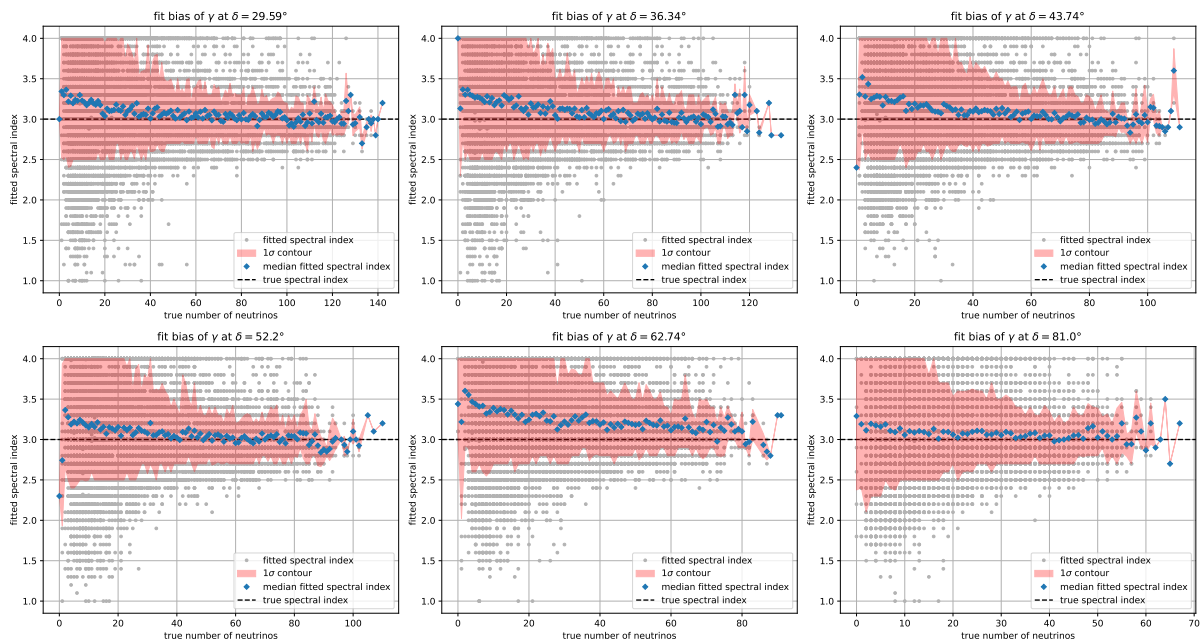


**Figure A.4:** Fit bias of the number of signal neutrinos for all simulated declinations with a true spectral index  $\gamma = 3.0$ . (cont.)

## Bibliography

- [1] IceCube Collaboration\*. “Evidence for High-Energy Extraterrestrial Neutrinos at the IceCube Detector”. In: *Science* 342.6161 (2013), p. 1242856. DOI: 10.1126/science.1242856. eprint: <https://www.science.org/doi/pdf/10.1126/science.1242856>. URL: <https://www.science.org/doi/abs/10.1126/science.1242856>.
- [2] M. G. Aartsen et al. “Time-Integrated Neutrino Source Searches with 10 Years of IceCube Data”. In: *Physical Review Letters* 124.5, 051103 (Feb. 2020), p. 051103. DOI: 10.1103/PhysRevLett.124.051103. arXiv: 1910.08488 [astro-ph.HE].
- [3] Theo Glauch. “The Origin of High-Energy Cosmic Particles: IceCube Neutrinos and the Blazar Case”. en. PhD thesis. Technische Universität München, 2021, p. 216. URL: <https://mediatum.ub.tum.de/1584755>.
- [4] Owen Gingerich. “Galileo, the Impact of the Telescope, and the Birth of Modern Astronomy”. In: *Proceedings of the American Philosophical Society* 155.2 (2011), pp. 134–141. ISSN: 0003049X. URL: <http://www.jstor.org/stable/23056830> (visited on 07/26/2024).
- [5] Karl G. Jansky. “Radio Waves from Outside the Solar System”. In: *Nature* 132.3323 (July 1933), p. 66. DOI: 10.1038/132066a0.
- [6] A. Hewish et al. “Observation of a Rapidly Pulsating Radio Source”. In: *Nature* 217.5130 (Feb. 1968), pp. 709–713. DOI: 10.1038/217709a0.
- [7] Riccardo Giacconi et al. “Evidence for x Rays From Sources Outside the Solar System”. In: *Physical Review Letters* 9.11 (Dec. 1962), pp. 439–443. DOI: 10.1103/PhysRevLett.9.439.
- [8] Klaus Pinkau. “History of gamma-ray telescopes and astronomy”. In: *Experimental Astronomy* 25.1-3 (Aug. 2009), pp. 157–171. DOI: 10.1007/s10686-009-9143-z.
- [9] Victor F. Hess. “Über Beobachtungen der durchdringenden Strahlung bei sieben Freiballonfahrten”. In: *Physikalische Zeitschrift* 13 (1912), pp. 1084–1091.
- [10] J. M. Weisberg, J. H. Taylor, and L. A. Fowler. “Gravitational waves from an orbiting pulsar”. In: *Scientific American* 245 (Oct. 1981), pp. 74–82. DOI: 10.1038/scientificamerican1081-74.

- [11] B. P. Abbott et al. “Observation of Gravitational Waves from a Binary Black Hole Merger”. In: *Physical Review Letters* 116.6, 061102 (Feb. 2016), p. 061102. DOI: 10.1103/PhysRevLett.116.061102. arXiv: 1602.03837 [gr-qc].
- [12] Raymond Davis, Don S. Harmer, and Kenneth C. Hoffman. “Search for Neutrinos from the Sun”. In: *Physical Review Letters* 20.21 (May 1968), pp. 1205–1209. DOI: 10.1103/PhysRevLett.20.1205.
- [13] K. Hirata et al. “Observation of a neutrino burst from the supernova SN1987A”. In: *Physical Review Letters* 58.14 (Apr. 1987), pp. 1490–1493. DOI: 10.1103/PhysRevLett.58.1490.
- [14] The IceCube Collaboration et al. “Search for a diffuse flux of astrophysical muon neutrinos with the IceCube 59-string configuration”. In: *arXiv e-prints*, arXiv:1311.7048 (Nov. 2013), arXiv:1311.7048. DOI: 10.48550/arXiv.1311.7048. arXiv: 1311.7048 [astro-ph.HE].
- [15] IceCube Collaboration\*† et al. “Observation of high-energy neutrinos from the Galactic plane”. In: *Science* 380.6652 (2023), pp. 1338–1343. DOI: 10.1126/science.adc9818. eprint: <https://www.science.org/doi/pdf/10.1126/science.adc9818>. URL: <https://www.science.org/doi/abs/10.1126/science.adc9818>.
- [16] IceCube Collaboration et al. “Evidence for neutrino emission from the nearby active galaxy NGC 1068”. In: *Science* 378.6619 (Nov. 2022), pp. 538–543. DOI: 10.1126/science.abg3395. arXiv: 2211.09972 [astro-ph.HE].
- [17] IceCube Collaboration et al. “Multimessenger observations of a flaring blazar coincident with high-energy neutrino IceCube-170922A”. In: *Science* 361.6398, eaat1378 (July 2018), eaat1378. DOI: 10.1126/science.aat1378. arXiv: 1807.08816 [astro-ph.HE].
- [18] L. Ju, D. G. Blair, and C. Zhao. “Detection of gravitational waves”. In: *Reports on Progress in Physics* 63.9 (Sept. 2000), pp. 1317–1427. DOI: 10.1088/0034-4885/63/9/201.
- [19] IceCube Collaboration et al. “IceCube Data for Neutrino Point-Source Searches Years 2008-2018”. In: *arXiv e-prints*, arXiv:2101.09836 (Jan. 2021), arXiv:2101.09836. DOI: 10.48550/arXiv.2101.09836. arXiv: 2101.09836 [astro-ph.HE].
- [20] Carmelo Evoli. *The Cosmic-Ray Energy Spectrum*. May 2023. DOI: 10.5281/zenodo.7948212. URL: <https://doi.org/10.5281/zenodo.7948212>.
- [21] Martina Stefanie Karl. “Unraveling the origin of high-energy neutrino sources: follow-up searches of IceCube alert events”. en. PhD thesis. Technische Universität München, 2022, p. 173.

- [22] Matteo Cerruti. “Leptonic and Hadronic Radiative Processes in Supermassive-Black-Hole Jets”. In: *Galaxies* 8.4, 72 (Oct. 2020), p. 72. DOI: 10.3390/galaxies8040072. arXiv: 2012.13302 [astro-ph.HE].
- [23] Pawan Kumar and Bing Zhang. “The physics of gamma-ray bursts & relativistic jets”. In: *Physics Reports* 561 (Feb. 2015), pp. 1–109. DOI: 10.1016/j.physrep.2014.09.008. arXiv: 1410.0679 [astro-ph.HE].
- [24] V. Beckmann and C. Shrader. “The AGN phenomenon: open issues”. In: *Proceedings of “An INTEGRAL view of the high-energy sky (the first 10 years)” - 9th INTEGRAL Workshop and celebration of the 10th anniversary of the launch (INTEGRAL 2012). 15-19 October 2012. Bibliotheque Nationale de France. Jan. 2012*, 69, p. 69. DOI: 10.22323/1.176.0069. arXiv: 1302.1397 [astro-ph.HE].
- [25] P. Padovani et al. “Active galactic nuclei: what’s in a name?” In: *Astronomy and Astrophysics Reviews* 25.1, 2 (Aug. 2017), p. 2. DOI: 10.1007/s00159-017-0102-9. arXiv: 1707.07134 [astro-ph.GA].
- [26] A. Azzollini et al. In: *Astronomy & Astrophysics* (submitted).
- [27] P. N. Best and T. M. Heckman. “On the fundamental dichotomy in the local radio-AGN population: accretion, evolution and host galaxy properties”. In: *Monthly Notices of the RAS* 421.2 (Apr. 2012), pp. 1569–1582. DOI: 10.1111/j.1365-2966.2012.20414.x. arXiv: 1201.2397 [astro-ph.CO].
- [28] P. Giommi et al. “A simplified view of blazars: clearing the fog around long-standing selection effects”. In: *Monthly Notices of the RAS* 420.4 (Mar. 2012), pp. 2899–2911. DOI: 10.1111/j.1365-2966.2011.20044.x. arXiv: 1110.4706 [astro-ph.CO].
- [29] M. G. Aartsen et al. “The IceCube Neutrino Observatory: instrumentation and online systems”. In: *Journal of Instrumentation* 12.3 (Mar. 2017), P03012. DOI: 10.1088/1748-0221/12/03/P03012. arXiv: 1612.05093 [astro-ph.IM].
- [30] R. L. Workman et al. “Review of Particle Physics”. In: *Progress of Theoretical and Experimental Physics* 2022 (2022), p. 083C01. DOI: 10.1093/ptep/ptac097.
- [31] M. G. Aartsen et al. “Astrophysical neutrinos and cosmic rays observed by IceCube”. In: *Advances in Space Research* 62.10 (Nov. 2018), pp. 2902–2930. DOI: 10.1016/j.asr.2017.05.030. arXiv: 1701.03731 [astro-ph.HE].
- [32] M. G. Aartsen et al. “Measurement of the multi-TeV neutrino interaction cross-section with IceCube using Earth absorption”. In: *Nature* 551.7682 (Nov. 2017), pp. 596–600. DOI: 10.1038/nature24459. arXiv: 1711.08119 [hep-ex].
- [33] George Casella and Roger Berger. *Statistical Inference*. Duxbury Resource Center, June 2001. ISBN: 0534243126.

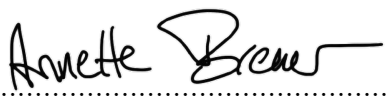
- [34] MessMapp Group. *internal note*.
- [35] Sara Buson et al. “Beginning a Journey Across the Universe: The Discovery of Extragalactic Neutrino Factories”. In: *Astrophysical Journal Letters* 933.2, L43 (July 2022), p. L43. DOI: 10.3847/2041-8213/ac7d5b. arXiv: 2207.06314 [astro-ph.HE].
- [36] M. G. Aartsen et al. “All-sky Search for Time-integrated Neutrino Emission from Astrophysical Sources with 7 yr of IceCube Data”. In: *Astrophysical Journal* 835.2, 151 (Feb. 2017), p. 151. DOI: 10.3847/1538-4357/835/2/151. arXiv: 1609.04981 [astro-ph.HE].
- [37] E. Massaro et al. “The 5th edition of the Roma-BZCAT. A short presentation”. In: *Astrophysics and Space Science* 357.1, 75 (May 2015), p. 75. DOI: 10.1007/s10509-015-2254-2. arXiv: 1502.07755 [astro-ph.HE].
- [38] R. Abbasi et al. “Improved Characterization of the Astrophysical Muon-neutrino Flux with 9.5 Years of IceCube Data”. In: *Astrophysical Journal* 928.1, 50 (Mar. 2022), p. 50. DOI: 10.3847/1538-4357/ac4d29. arXiv: 2111.10299 [astro-ph.HE].
- [39] Chiara Bellenghi et al. “Correlating High-energy IceCube Neutrinos with 5BZCAT Blazars and RFC Sources”. In: *Astrophysical Journal, Letters* 955.2, L32 (Oct. 2023), p. L32. DOI: 10.3847/2041-8213/acf711. arXiv: 2309.03115 [astro-ph.HE].
- [40] Chiara Bellenghi, Martina Karl, and Martin Wolf. “Extending SkyLLH software for neutrino point source analyses with 10 years of IceCube public data”. In: *arXiv e-prints*, arXiv:2308.12733 (Aug. 2023), arXiv:2308.12733. DOI: 10.48550/arXiv.2308.12733. arXiv: 2308.12733 [astro-ph.HE].

# Declaration of originality

I declare that I have authored this thesis independently, that I have not used other than the declared sources/resources, and that I have explicitly marked all material that has been quoted either literally or by content from the used sources. I hereby also declare that my thesis has not been prepared for another examination or assignment, either wholly or excerpts thereof.

Hiermit erkläre ich, dass ich die alleinige Autorin dieser Arbeit bin und keine anderen Quellen oder Hilfen, außer den aufgeführten, verwendet wurden. Weiterhin erkläre ich, dass ich die Arbeit Andere durch detaillierte Referenzen anerkannt habe. Ebenso erkläre ich hiermit, dass meine Arbeit nicht für eine andere Prüfung oder Aufgabe, weder vollständig noch in Auszügen, vorbereitet wurde.

Würzburg, October 2, 2024

Annette Bremer  .....